DESIGN AND IMPLEMENTATION OF AN ELECTRONIC CONTROL AND IMAGE ACQUISITION SYSTEM FOR LASER SCANNING CONFOCAL MICROSCOPY

by

Gökhan Gümüş

B.S., Electrical and Electronics Engineering, TOBB University of Economics and Technology, 2013

Submitted to the Institute for Graduate Studies in
Science and Engineering in partial fulfillment of
the requirements for the degree of
Master of Science

Graduate Program in Electrical and Electronics Engineering
Boğaziçi University
2016

ACKNOWLEDGEMENTS

First of all, I would like to express my gratitude to my thesis supervisor Assist. Prof. Faik Başkaya. He honored me by accepting me as a master student under his supervision.

I would like to thank to my thesis co-supervisor Assist. Prof Baykal Sarıoğlu for his patience and understanding while solving my problems and listening my ideas. His ultimate guidance made this thesis possible. He also taught me how to write an academic paper and how to be a better researcher which are as valuable as my thesis for me.

Also, I would like to thank Assist. Prof. Yiğit Dağhan Gökdel not only for his recommendations about my thesis but also for encouraging me to produce academic work. He always showed his support throughout the last two years.

I would like to thank Assoc. Prof. Arda Deniz Yalçınkaya and Assoc. Prof. Ali Emre Pusane for their attendance to my thesis committee.

I would like to thank all of my friends for showing their support along this journey and making my days more enjoyable.

Lastly, but most importantly, I would like to thank to my family who showed their endless support throughout my master's degree studies. Additionally, I am thankful to them for being my alarm clock. I could not attend morning classes, if it weren't for them.

ABSTRACT

DESIGN AND IMPLEMENTATION OF AN ELECTRONIC CONTROL AND IMAGE ACQUISITION SYSTEM FOR LASER SCANNING CONFOCAL MICROSCOPY

In this thesis, an electronic control and image acquisition system for a laser scanning confocal microscope (LSCM) is presented. The system is controlled from a graphical user interface (GUI) via a data acquisition (DAQ) card. GUI is designed and programmed on MATLAB software. Software of the system consists of two parts: generation of the actuation signal and image acquisition and formation. Signals which actuate scanning units to scan the target in LSCM system can be generated by using GUI. The LSCM system is designed in two different configurations: In one configuration, a galvanometer is utilized and in the other one, utilized scanning unit is a 3D printed micro-scanner. Afterwards, image acquisition and display process starts. Two different scanning methods, which are raster scanning and Lissajous scanning, are employed to scan the target. Scanning units steer laser beams to the target. Reflected laser beams from the target are acquired by a photo multiplier tube (PMT) that generates current values according to the power of the reflected laser beam. The current values are converted to voltage values using a resistor and then digitized using a DAQ card. The acquired voltage values are mapped between 0 and 255 pixel intensity values according to previously calibrated maximum and minimum voltage values. After all the pixel values are gathered in this manner, a 2D image is constructed and displayed on the GUI of the MATLAB program. Successful operation of the proposed software based GUI system is demonstrated by constructing images from USAF 1951 negative resolution test target. Additionally, successful results on specimens like onion epidermal cells, red blood cells, bacteria cells, yeast cells, chicken skin are provided.In order to improve image quality, denoising with wavelets is applied on resulting images.

ÖZET

LAZER TARAMALI KONFOKAL MİKROSKOP İÇİN ELEKTRONİK KONTROL VE GÖRÜNTÜ ALMA SİSTEMİ TASARIMI VE UYGULAMASI

Bu tezin içeriğinde, lazer taramalı konfokal mikroskop sistemi için elektronik kontrol ve görüntü alma sistemi sunulmuştur. Sistem veri toplama kartı aracılığıyla MATLAB yazılımı üzerinde tasarlanıp programlanan bir kullanıcı arayüzünden kontrol edilmektedir. Sistem iki bölümden oluşmaktadır; (1) hareketlendirme sinyallerinin oluşturulması ve (2) görüntü elde edilmesi. Lazer taramalı konfokal mikroskop sistemindeki tarayıcı birimlerin hareketini sağlayan hareketlendirme sinyalleri, kullanıcı arayüzünden oluşturulmaktadır. Sistem tarayıcı birim olarak galvanometre veya üç boyutlu yazıcı kullanılarak üretilmiş mikro-tarayıcılar kullanılmaktadır. Daha sonra görüntü alma işlemi başlatılır. Sistemde hedefi taramak için ızgara tarama ve Lissajous tarama metodları kullanılmıştır. Tarayıcı birimler lazer ışınlarını hedefe yöneltir. Hedeften yansıyan lazer ışınları bir foto multiplikatör tüp tarafından toplanır. Foto multiplikatör tüp yansıyan ışınların gücüne göre akım değerleri üretir. Bu akım değerleri bir direnç vasıtasıyla gerilim değerlerine çevirilir ve bu voltaj değerleri veri toplama kartı tarafından toplanır. Toplanan gerilim değerleri daha önceden belirlenen maksimum ve minimum gerilim değerlerine göre 0 ile 255 arasındaki piksel değerlerine atanır. Tüm piksel değerleri bu şekilde belirlendikten sonra iki boyutlu görüntü oluşturulur ve MATLAB yazılımındaki kullanıcı arayüzünde gösterilir. Sistemin başarılı deneyleri USAF 1951 çözünürlük hedefinden alınan görüntülerle gösterilmiştir. Buna ek olarak, soğan zarı, alyuvar hücreleri, bakteri hücreleri, maya hücreleri ve tavuk derisi gibi örneklerden alınan görüntüler de sunulmuştur. Alınan görüntülerin kalitesinin arttırılması amacıyla, alınan görüntüler üzerinde dalgacıklar kullanılarak gürültü giderimi yapılmıştır.

TABLE OF CONTENTS

ACKNOWLEDGEMENTS . . . iii
ABSTRACT . . . iv
ÖZET . . . v
LIST OF FIGURES . . . viii
LIST OF TABLES . . . xii
LIST OF SYMBOLS . . . xiii
LIST OF ACRONYMS/ABBREVIATIONS . . . xvi
1. INTRODUCTION . . . 1
2. SYSTEM DESCRIPTION . . . 6
2.1. System Components . . . 6
2.1.1. Data Acquisition Card . . . 6
2.1.2. Photo Multiplier Tube . . . 7
2.1.3. Micro-Scanner . . . 9
2.1.4. Power Amplifier . . . 13
2.1.5. Galvanometer . . . 15
2.2. Galvanometer Based LSCM System . . . 16
2.3. Micro-Scanner Based LSCM System . . . 17
3. MICROSCOPE SOFTWARE . . . 21
3.1. Signal Generation . . . 21
3.2. Image Acquisition . . . 24
3.2.1. Raster Scanning . . . 24
3.2.2. Lissajous Scanning . . . 27
3.3. Noise Reduction . . . 33
3.3.1. Discrete Wavelet Transform . . . 35
3.3.2. Thresholding Method and Selection of the Threshold Value . . . 39
4. EXPERIMENTAL RESULTS . . . 44
4.1. Acquired Images From LSCM System . . . 44
4.2. Results of Denoising Process . . . 53
5. CONCLUSION . . . 60

REFERENCES 62

LIST OF FIGURES

Figure 1.1. Confocal image (A) compared with a conventional epifluorescence image (B) of a similar region of a whole mount of a butterfly pupal wing stained with propidium iodide [19]. 2

Figure 1.2. Comparison of A) LSCM and B)WFM Performance in Imaging of a Thick Tissue [21] (Scale bar is 50 μm). 3

Figure 1.3. Basic Configuration of Confocal Systems. 4

Figure 2.1. Diagram of Photo multiplier Tube's Architecture [45]. 7

Figure 2.2. Drawings of the micro-scanners parametrically showing their dimensions. a) Design A b) Design B [37]. 9

Figure 2.3. Mode shapes of Design A and Design B. a) Out-of-plane bending mode at 137 Hz for Design A. b) Torsion at 335 Hz for Design A. c) Out-of-plane bending mode at 126 Hz for Design B. d) Torsion at 275 Hz for Design B [37]. 11

Figure 2.4. Frequency response of micro-scanners for different electrocoil driving current values a) Design A b) Design B [37]. 14

Figure 2.5. Power Amplifier Circuit Schematic. 15

Figure 2.6. AC Sweep Simulation Results for Power Amplifier. 15

Figure 2.7. Block diagram of the proposed system. 16

Figure 2.8. Flowchart of the MATLAB program for LSCM. 18

Figure 2.9. Block diagram of the proposed system. 19

Figure 3.1. GUI on MATLAB and example waves generated by DAQ Card with f= 100 Hz and V_{pp}=4. Harmonic wave is composed of 100 Hz and 1 kHz sinusoidal wave. 22

Figure 3.2. GUI on MATLAB. 23

Figure 3.3. Raster Scan Tracing: (1) Scan Line (2) Horizontal Retrace (3) Vertical Retrace. 25

Figure 3.4. Raster Scanning Algorithm 27

Figure 3.5. Lissajous Curves Examples for $\frac{1}{2}, \frac{3}{2}, \frac{3}{4} and \frac{5}{4}$ values of $\frac{f_x}{f_y}$ from Left to Right [47]. 28

Figure 3.6. Fill Rates of Lissajous Scanning for Different FOV Values. 31

Figure 3.7. Maximum Fill Rates of Lissajous Scanning for Different Frame Rates. 32

Figure 3.8. Lissajous Scanning Algorithm 33

Figure 3.9. Lissajous patterns for various scan frequencies and frame rates. Horizontal and vertical frequencies for (a)-(d) and (e)-(h) are f_x = 100 Hz, f_y = 350 Hz and f_x = 101 Hz, f_y = 351 Hz respectively. Frame rates from (a) to (d) and from (e) to (h) are 1, 5, 10 and 20 Hz. Fill rates for (a)-(d) are %13.4 and from (e) to (h) are %30.7, %46.7, %79.7 and %100, respectively. 34

Figure 3.10. Analysis and synthesis of a 1D signal with subband coding. (a) DWT and Inverse DWT of 1D signal, (b)DWT tree, (c)Wavelet packet tree 37

Figure 3.11. Two level Discrete Wavelet Transform 39

Figure 4.1. Test Setup. 44

Figure 4.2. USAF-1951 Resolution Target and Scanned Part of the USAF Resolution Target. 45

Figure 4.3. Acquired Image From the Resolution Target. 46

Figure 4.4. Acquired Images from 16 Different Layers of Onion Skin. 47

Figure 4.5. Yeast Cells a) Under LSCM b) Under Light Microscope. 48

Figure 4.6. Chicken Skin Sample Under a) LSCM b) Vivascope 3000. 48

Figure 4.7. Images Taken From Two Different Layers of an Onion Epidermal Cell. 49

Figure 4.8. Bacteria Cells Under LSCM System. 50

Figure 4.9. Red Blood Cells Under LSCM System. 50

Figure 4.10. Acquired Image from Resolution Target by Using Lissajous Scanning with Frequency Values $f_x = 101$ Hz and $f_y = 100$ Hz. 51

Figure 4.11. Resulting Image of Lissajous Scanning on Resolution Target with Frequency Values $f_x = 101$ Hz and $f_y = 100$ Hz. 52

Figure 4.12. Resulting Image of Lissajous Scanning with 3D Printed Micro-Scanner on Resolution Target with Frequency Values $f_x = 238$ Hz and $f_y = 113$ Hz. 52

Figure 4.13. a) Original Lena Image (512x512) b) Noisy Lena Image $\sim N(0, \sigma^2)$ $\sigma = 25$. 53

Figure 4.14. Resulting Denoised Image of GME and Sym15 Wavelet Method $PSNR_{\text{diff}} = 5.5773\ dB$. 55

Figure 4.15. Resulting Denoised Image of LDME and Sym15 Wavelet Method $PSNR_{\text{diff}} = 3.3021\ dB$. 56

Figure 4.16. Resulting Denoised Image of DDME and Sym8 Wavelet Method $PSNR_{\text{diff}} = 9.0126\ dB$. 57

Figure 4.17. Denoising Results with a) Hard Thresholding b) Soft Thresholding 58

Figure 4.18. a) Original Image Acquired From Bacteria Cells Sample b) Denoised Image 58

Figure 4.19. a) Original Image Acquired From Red Blood Cells Sample b) Denoised Image 59

Figure 4.20. a) Original Image Acquired From Onion Epidermal Sample b) Denoised Image 59

LIST OF TABLES

Table 2.1. Dimensions of the scanners. 10

Table 3.1. Maximum Fill Rates for Different Frame Rates and Frequency Pairs that Provide the Maximum Fill Rate Values. 32

Table 4.1. $PSNR_{\text{diff}}$ Values for GME 54

Table 4.2. $PSNR_{\text{diff}}$ Values for LDME 55

Table 4.3. $PSNR_{\text{diff}}$ Values for DDME 56

LIST OF SYMBOLS

$a_{\mathrm{j,\,k}}$	Transform coefficients
a_k	Analysis coefficients
B	Magnetic field strength
C	Current amplification
D	Total number of dynodes
f_{fast}	Fast scan frequency
$\mathrm{f_o}$	Resonant frequency for the out-of-plane mode of Design A
f_{s}	Sampling rate
f_{slow}	Slow scan frequency
$\mathrm{f_t}$	Resonant frequency for the torsion mode of Design A
f_{x}	Driving frequencies in the x direction
f_{y}	Driving frequencies in the y direction
G	Shear modulus of the material
g_{n}	Gain of the nth dynode
I	Amplitude of the driving current signal
I_{h}	Image height
I_{w}	Image width
J_{eff}	Effective moment of inertia (MOI) of the scanner
J_{f}	MOI of the flexure part
J_{fi}	MOI of inner flexure
J_{fo}	MOI of outer flexure
J_{g}	MOI of gimbal
J_{m}	MOI of the mirror part
J_{zz}	Second moment of inertia of the cross section of the flexure
k	Torsional stiffness
k_{o}	Spring constant for out-of-plane mode
k_{t}	Spring constant for torsion mode
L_{f}	Length of the flexure

M_{eff}	Effective mass of the scanner
M_{f}	Mass of flexure part
M_{fi}	Mass of inner flexure
M_{fo}	Mass of outer flexure
M_{g}	Mass of gimbal
M_{m}	Mass of mirror part
n_{a}	Number of electrons collected
n	Turn density of the coil
n_{k}	Number of photoelectrons which strike the first dynode
N_{pixels}	Number of pixels in a row
N_{rows}	Number of rows of resulting image
N_t	Noise in transform domain
P	Total number of pixels in image
t	time
t_{acq}	Image acquisition time
t_{op}	Process time of the MATLAB program
w	Transformation coefficients
W	2D DWT operator
W^{-1}	Inverse 2D DWT operator
w_r	FWHM resolution value
X	Maximum value $x(t)$ could get
$\hat{x}$	Estimation of original image x from noisy image y
$x_{\text{i, j}}$	Original image
X_t	Original image in transform domain
Y	Maximum value $y(t)$ could get
$\widehat{Y}$	Thresholded wavelet coefficients
$y_{\text{i, j}}$	Noisy image
Y_t	Noisy image in transform domain
δ	Threshold value
$\epsilon_{\text{i, j}}$	i.i.d. zero mean white Gaussian noise with standard deviation σ

η^{H}	Hard thresholding rule
η^{S}	Soft thresholding rule
λ	Wavelength of the utilized laser
μ	Mean
$\hat{\mu}$	Fixed estimate of μ based on the observations
μ	Permeability of the core material
σ	Standard deviation
$\hat{\sigma}$	Estimated Noise Standard Deviation
σ^2	Noise variance
ϕ_{x}	Phase shift in x
ϕ_{y}	phase shift in y
$\psi_{\mathrm{j,\,k}}$	Basis functions
ψ_{k}	Analyzing functions

LIST OF ACRONYMS/ABBREVIATIONS

1D	One Dimensional
2D	Two Dimensional
2P	Two Photon
3D	Three Dimensional
ADC	Analog Digital Converter
CM	Confocal Microscopy
DAQ	Data Acquisition Card
DDME	Detail Dependent Median Estimator
DWT	Discrete Wavelet Transform
FOV	Field-of-View
FPS	Frame Per Second
FWHM	Full Width Half Maximum
GME	Global Median Estimator
GUI	Graphical User Interface
LDME	Level Dependent Median Estimator
LSCM	Laser Scanning Confocal Microscopy
LSM	Laser Scanning Microscope
MEMS	Microelectromechanical System
MOI	Moment of Inertia
MSE	Mean Squared Error
NA	Numerical Aperture
OCT	Optical Coherence Tomography
PMT	Photo Multiplier Tube
PSNR	Peak Signal to Noise Ratio
SURE	Stein's Unbiased Risk Estimate
WFM	Wide Field Microscope

1. INTRODUCTION

Developments in optical fiber, MEMS and computing technologies have led up to minimum invasive and cheap optical imaging approaches such as optical coherence tomography (OCT) [1–3], two photon microscopy (2P) [4–6] and confocal microscopy (CM) [7–9].

Confocal microscopy is a well-established method for obtaining high resolution images of biological tissue [10]. In this microscopy technique, in order to block away unwanted out-of-focus light, a spatial pinhole is located at the focal plane of the lens [11]. Due to this property, CM allows to obtain images with high contrast ratio. Additionally, with the optical slicing property of CM, approximately 400 μm deep of the targeted tissue can be seen. This property of CM makes three dimensional (3D) imaging possible. Its optical sectioning ability and in-depth imaging about a few hundred micrometers beneath the tissue surface enable precise diagnosis of pathological conditions in human body [12–15]. Images of human and mouse skin [9], colon tissue [7], oral mucosa [16], GI-tract [17] and colon tissue of a rat [18] are acquired with CM. Since the resolution achieved by the LSCM is a little better than that achieved in a conventional wide field light microscope (theoretical maximum resolution of 0.2 μm), but not as great as that in the transmission electron microscope (0.1 nm), it has bridged the gap between these two commonly used techniques [19]. Comparison between images acquired with conventional light microscope and confocal microscope from same specimen can be seen in Figure 1.1. In this comparison, it can be clearly seen that resolution of the nuclear detail is improved by employing confocal microscope. Additionally, comparison between images acquired with laser scanning confocal microscope and wide field fluorescence microscope (WFM) from same specimen can be seen in Figure 1.2.

All of the modern confocal imaging systems employ the principle of confocal imaging that Minsky patented in 1957 [19,20]. In Minsky's original confocal microscope the point source of light is produced by a pinhole placed in front of a zirconium arc

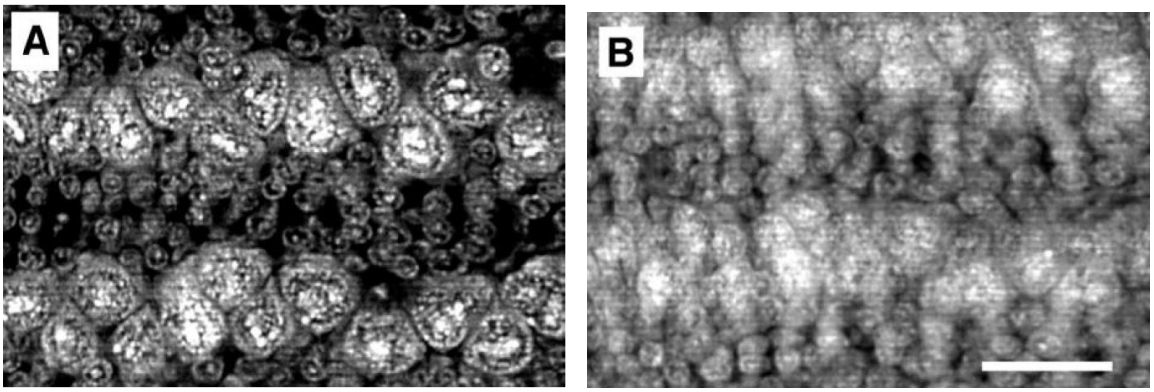

Figure 1.1. Confocal image (A) compared with a conventional epifluorescence image (B) of a similar region of a whole mount of a butterfly pupal wing stained with propidium iodide [19].

source. The point of light is focused by an objective lens into the specimen, and light that passes through it is focused by a second objective lens at a second pinhole, which has the same focus as the first pinhole, i.e., it is confocal with it. Any light that passes through the second pinhole strikes a low noise photo multiplier, which produces a signal that is directly proportional to the brightness of the light. The second pinhole prevents light from above or below the plane of focus from striking the photo multiplier. This is the key to the confocal approach, namely the elimination of out-of-focus light or "flare" in the specimen by spatial filtering. Minsky also described a reflected light version of the microscope that uses a single objective lens and a dichromatic mirror arrangement. Basic configuration of most modern confocal systems can be seen in Figure 1.3.

Despite the fact that, galvanometers are utilized as the scanning units in early and conventional laser scanning microscopes (LSM) [22], nowadays, micro-scanners are utilized as scanning units instead of galvanometers to make LSM systems more compact and portable [7, 23, 24]. Micro-scanners move along two orthogonal axes namely fast scan axis and slow scan axis. Therefore, they deliver two dimensional (2D) orthogonal scanning process. In order to actuate micro-scanner, there are several different actuation techniques such as electrothermal [25], electrostatic [26], piezoelectric [27] and electromagnetic [28]. Every actuation technique has some advantages and disadvantages over one another depending on their micro-scanner applications. However, electromagnetic actuation technique is more advantageous than other actuation techniques because of its larger scanning angle and smaller driving voltages. This property

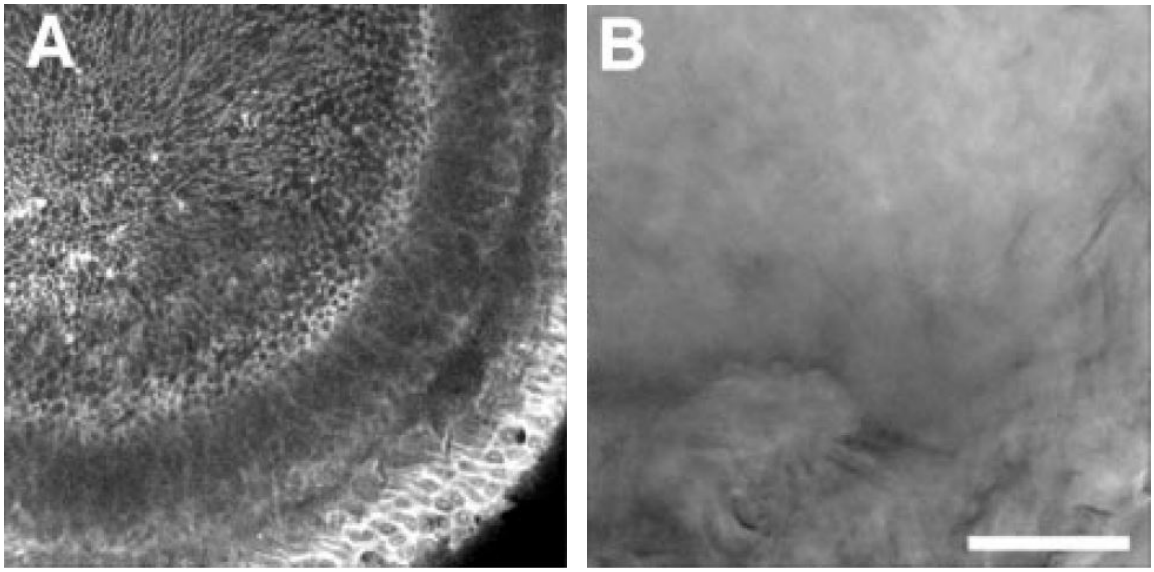

Figure 1.2. Comparison of A) LSCM and B)WFM Performance in Imaging of a Thick Tissue [21] (Scale bar is 50 μm).

makes electromagnetic actuation technique more preferable choice to be used in medical applications where safety of patient is important [29, 30].

3D printing technology is becoming more popular in various research areas day by day. Different kind of sensors and actuators are produced for various applications such as force sensor which is used for robotic manipulation and robotic catheter instrument [31,32] and custom optical elements which are embedded in interactive devices to open up new possibilities for interaction [33]. 3D additive manufacturing techniques have utilized to make 3D electrical components, such as resistors, capacitors, and inductors, as well as circuits and passive wireless sensors [34]. Arbitrarily formed capacitive sensors are manufactured by using 3D printing technology [35]. Quantum dot light-emitting diodes are also an example of 3D printed devices [36].

In this thesis, galvanometer and 3D printed micro-scanners [37] are utilized in two different configurations as scanning unit. Target is scanned with both of the scanning techniques which are raster and Lissajous scanning [38] when galvanometer is utilized. On the other hand, when micro-scanners are utilized, to obtain a meaningful image of a target, Lissajous scanning is employed. Because in raster scanning, resolution of acquired image depends on the ratio of fast and slow scan frequencies and with micro-

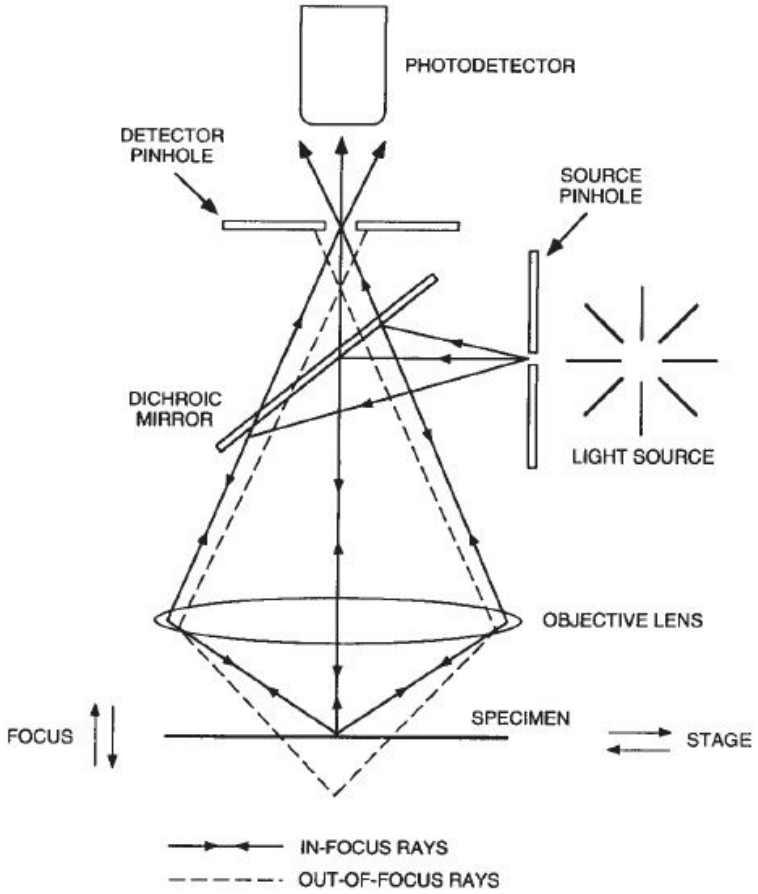

Figure 1.3. Basic Configuration of Confocal Systems.

scanner the ratio between fast and slow scan frequencies could be very low. Therefore, acquiring a meaningful image could be prevented. Lissajous scanning patterns are often employed in laser scanning systems where the more common raster scanning pattern is impractical. This is often the case in miniaturized laser scanning microscopes using microelectromechanical system (MEMS) scanning mirrors or piezoelectric fiber scanners for beam scanning [4, 5, 15, 39–41]. Reason of that is with appropriate scanning frequencies desired field-of-view (FOV) can be scanned completely by Lissajous patterns. Usage of Lissajous scanning has led up to rapid imaging in atomic force microscopy and multiphoton microscopy [4, 42]. Coupled with image interpolation algorithms, 2D Lissajous scanning provides frame rate above 1 kHz [43].

In this thesis, an electronic system for a LSCM which is controlled through a Data Acquisition (DAQ) card is proposed. Entire operation of LSCM system can be controlled from a graphical user interface (GUI) which is designed and programmed

on MATLAB environment. Through DAQ card, the system does not only create the required driving signal which actuate micro-scanner or galvanometer, but also is responsible from the image acquisition part by both serially collecting the laser intensity data and transforming it to a meaningful microscopy image. Additionally, to eliminate noise from the acquired microscopy image, wavelets are employed [44].

This thesis is organized as follows. In Chapter 2, operation principle and components of the system are explained. In Chapter 3, information about designed GUI, scanning methods, details on image denoising with wavelets and steps of the employed denoising algorithm is given. In Chapter 4, images which are acquired from designed system and results of denoising process are presented and evaluated. Finally, Chapter 5 concludes with opinions and directions for the future works.

2. SYSTEM DESCRIPTION

In this thesis, an electronic system for a LSCM which is controlled through a DAQ card is proposed. Entire operation of LSCM system can be controlled from a GUI which is designed and programmed on MATLAB environment. Through DAQ card, the system does not only generate the required driving signal which actuate micro-scanner or galvanometer, but also is responsible from the image acquisition part by both serially collecting the laser intensity data and transforming it to a meaningful microscopy image. In the system, DAQ card is utilized to generate driving signals which actuate scanning units of the system and to acquire scanning data from photo multiplier tube which is utilized as a sensor. Galvanometer and 3D printed micro-scanners are utilized as scanning units which steer laser beams with 653 nm wavelength into desired scanning area on target. In order to provide sufficient current value to drive micro-scanner properly, an amplification circuit with LM 386 power amplifier is also utilized in the system. In the following part, components and operation principles of the system is explained in detail.

2.1. System Components

2.1.1. Data Acquisition Card

Data Acquisition(DAQ) cards sample signals that measure real world physical conditions and convert them to digital numeric values which can be manipulated by computer. The process can be summarized in two steps:

In the first step, real world physical conditions must be converted electrically expressible values such as current or voltage via sensors. Microphones and photocells can be given as examples to sensors. In this thesis, H10720 Series photo multiplier tube is utilized as sensor.

In the second step, analog signals which are acquired by sensors are sampled and are transmitted to computer. Sampling process is handled by analog digital converter (ADC) which is inside of the DAQ card. To acquire and sample analog signals analog input channel of the DAQ card must be utilized. If incoming signal is already converted digital numeric values by sensors, these values can be acquired directly from digital input channel of the DAQ card. Additionally, by means of components like timer and counter, the DAQ cards make data acquiring and generating more convenient.

In this thesis, National Instrument's NI- USB 6356 model DAQ card is utilized. The NI- USB 6356 has 1.25 MHz sampling rate, 8 analog inputs, 2 analog outputs and 24 digital input-output (I/O) lines. Its maximum output voltage is 10 volts and maximum output current is 5 miliamperes.

2.1.2. Photo Multiplier Tube

In this thesis, as a sensor photo multiplier tube (PMT) is utilized. PMT is light sensitive sensor which offers internal high gain. In low light intensity cases, PMTs are very useful because of the high gain property of them. Photocathode, dynodes, an anode, an external power supply and an external current are five main parts of PMT. They are shown in Figure 2.1.

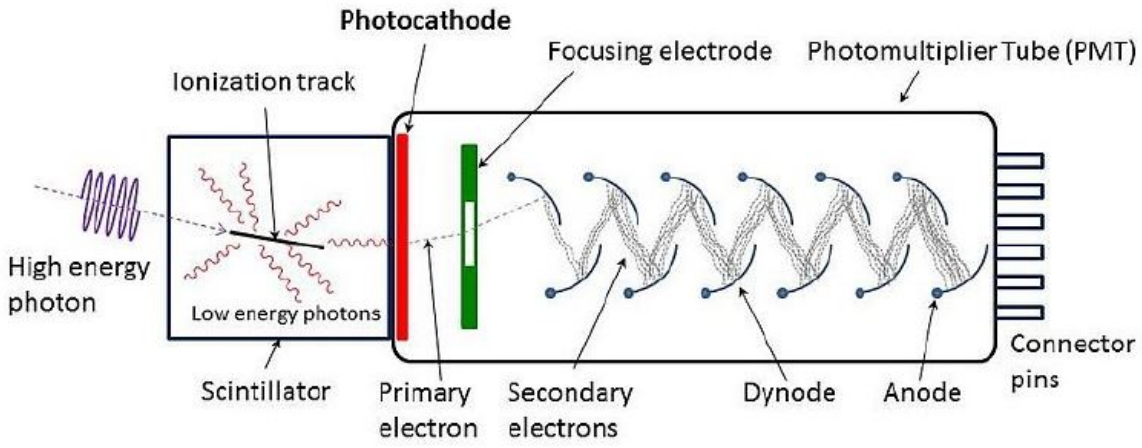

Figure 2.1. Diagram of Photo multiplier Tube's Architecture [45].

Light moves through a quartz or glass window and afterwards reaches to photocathode. Photocathode is a photo emissive surface. When a photon which has a sufficient energy level hits to the photocatode, an electron is released. This is named as photoelectric effect. Thereafter, the electron strikes to dynodes. Dynodes are array of electrodes between anode and cathode inside the PMT. They are utilized in order to speed up electrons. Each dynode holds more positive voltage than the previous one. For this reason, each dynode applies a more powerful pulling force on electrons than the previous one. In order to create electric field between the anode and the cathode, an external power supply is utilized. Electrons gain kinetic energy due to the electric field. Hence, more electrons are released after each dynode and the electrons reach much higher energy level after each emission. This process ends when electrons reach to the anode. The anode gathers released electrons. Even though one electron is emitted at the star of the process, a lot of electrons are gathered at the end of the process. External current meter quantifies the number of gathered electrons at the anode.

According to [34], generated current by PMT depends on two factors; the number of the captured electrons and the gain of the photo multiplier tube. Relation between them can be expressed as,

$$n_{\mathrm{a}} = n_{\mathrm{k}} \prod_{n=1}^{D} g_{\mathrm{n}} \tag{2.1}$$

$$C = \frac{n_{\mathrm{a}}}{n_{\mathrm{k}}} \tag{2.2}$$

where n_{k} is the number of photoelectrons which strike the first dynode, g_{n} is the gain of the nth dynode, n_{a} is the number of electrons collected, D is total number of dynodes and C the current amplification.

In this thesis, H10720 Series photo multiplier tube is utilized. Maximum output current of this device is 100 microamperes when 1 volt control voltage is applied. Recommended input voltage range is between 4.5 and 5.5 volts. In the LSCM system, PMT collects reflected laser beams from target and generates current according to power of the reflected laser beam. The output current value is converted voltage value by using a resistor. The voltage value is acquired by DAQ Card afterwards.

2.1.3. Micro-Scanner

In the proposed LSCM system, a 3D printed 2D micro-scanner is utilized to reflect laser beams to the target. The 2D micro-scanner scans target along two orthogonal directions namely fast and slow scan axis. Slow and fast scan resonant frequencies of the micro-scanner must be precisely triggered in order to start actuation of the micro-scanner. Detailed explanation of actuation of the micro-scanner takes place in subsection 2.1.4. Two different designs for the 2D micro-scanner are utilized in the setup. They will be called as Design A and Design B after this point. Detailed information is given about the design of these micro-scanners in the following part based on [37].

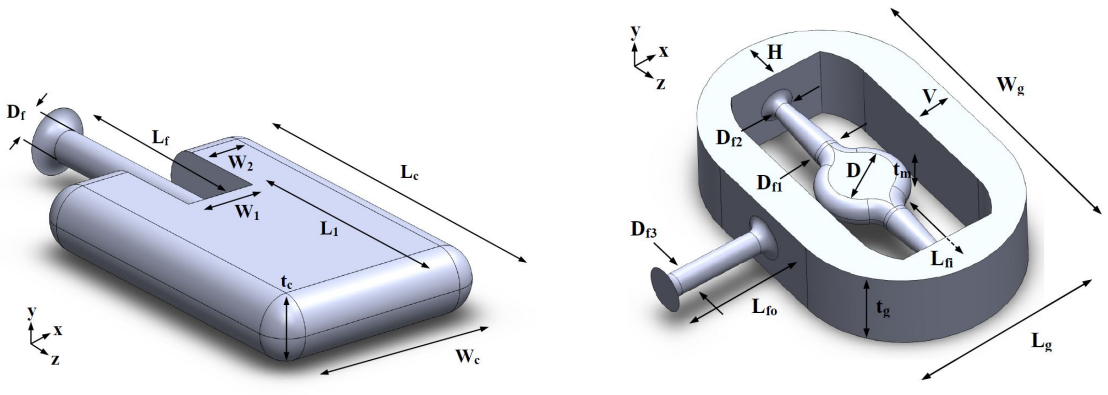

(a) (b)

Figure 2.2. Drawings of the micro-scanners parametrically showing their dimensions. a) Design A b) Design B [37].

The material of 3D printed micro-scanners is a photopolymer which is named as VeroClear. Additionally, to obtain large displacements four Neodymium based magnets are placed on micro-scanners. To decrease the stress at the junction points, cross section of flexures are made circular. Drawings which show shapes and parametric dimensions of micro-scanners can be seen in Figure 2.2

Numerical values for the dimensions which are defined parametrically in Figure 2.2 are shown in Table 2.1.

Table 2.1. Dimensions of the scanners. (all in mm) [37].

	Dimensions											
Design A	D_f	L_f	L_c	L_1	W_c	W_1	W_2	t_c				
	1	8	12	8	8	2.5	1.75	2				
Design B	D	D_{f1}	D_{f2}	D_{f3}	L_{fi}	L_{fo}	L_g	H	V	W_g	t_g	t_m
	4.0	1.2	0.7	1.0	3.5	5.0	10.0	2.0	16.0	3.5	1.2	

To obtain Lissajous patterns, combination of second and third modes are used which are named as out-of-plane bending movement and torsion respectively. Out-of-plane bending movement of the Design A and Design B is at 137 and 126 Hz respectively. Torsion, which is the movement around flexure is observed for Design A and Design B at 335 and 275 Hz respectively. Movement shapes for micro-scanners are shown in Figure 2.3.

In the design process, scanners are modeled as spring-mass system. Flexure part of the Design A can be thought as a spring and mirror part of the Design A can be thought as mass. For the torsion mode of Design A, resonant frequency can be approximated as a simple harmonic oscillator and expressed as,

$$f_t = \frac{1}{2\pi}\sqrt{\frac{k_t}{J_{eff}}} \tag{2.3}$$

where k_t is the spring constant and J_{eff} is the effective moment of inertia (MOI) of the scanner. Design A is composed of a mirror part and flexure. Hence, its effective MOI

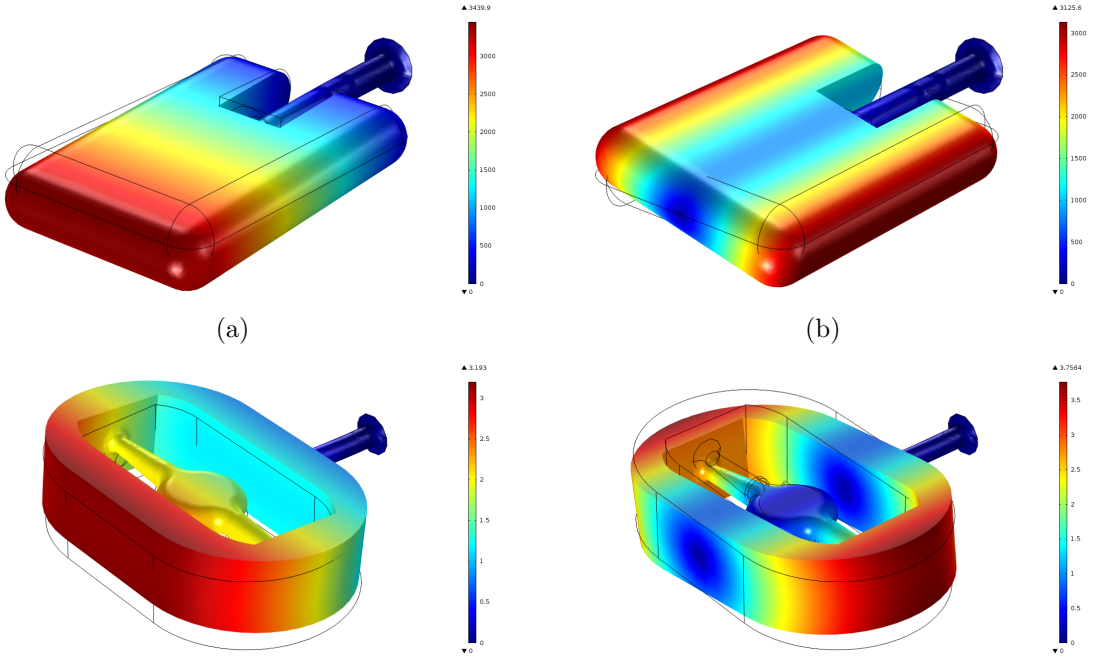

Figure 2.3. Mode shapes of Design A and Design B. a) Out-of-plane bending mode at 137 Hz for Design A. b) Torsion at 335 Hz for Design A. c) Out-of-plane bending mode at 126 Hz for Design B. d) Torsion at 275 Hz for Design B [37].

can be computed as,

$$J_{\text{eff}} = J_{\text{m}} + J_{\text{f}} \tag{2.4}$$

where J_{f} and J_{m} represent MOIs of the flexure and mirror part respectively. Additionally, in [46], spring constant of a beam which has a circular cross section is expressed as,

$$k_{\text{t}} = \frac{Gk}{L_{\text{f}}} \tag{2.5}$$

where G is shear modulus of the material, k is torsional stiffness and L_{f} is length of the flexure. On the other hand, for the out-of-plane bending movement of the Design

A resonant frequency can be calculated as,

$$f_{\mathrm{o}} = \frac{1}{2\pi}\sqrt{\frac{k_{\mathrm{o}}}{M_{\mathrm{eff}}}} \tag{2.6}$$

where M_{eff} is effective mass of the scanner. M_{eff} can be computed by using the expression,

$$M_{\mathrm{eff}} = M_{\mathrm{m}} + M_{\mathrm{f}} \tag{2.7}$$

where M_{f} and M_{m} are mass values for flexure part and mirror part of the scanner respectively. For the out-of-plane bending movement of Design A, spring constant formula is given as,

$$k_{\mathrm{o}} = \frac{3GJ_{\mathrm{zz}}}{{L_{\mathrm{f}}}^3} \tag{2.8}$$

where J_{zz} represents the second moment of inertia of the cross section of the flexure.

Resonant frequency for torsion movement of the Design B can be computed with Eq. (2.3) in the same manner with the Design A. Additionally, spring constant for Design B can be found by using Eq.(2.5). Effective MOI of the Design B is given as,

$$J_{\mathrm{eff}} = J_{\mathrm{m}} + J_{\mathrm{fo}} + J_{\mathrm{g}} + 2J_{\mathrm{fi}} \tag{2.9}$$

where J_{m}, J_{fo}, J_{g} and J_{fi} represent MOIs of the mirror, outer flexure, gimbal and inner flexure respectively. To calculate resonant frequency for out-of-plane bending movement of Design B Eq. (2.6) can be used. In Design B case effective mass is given

as,

$$M_{\text{eff}} = M_{\text{m}} + M_{\text{fo}} + M_{\text{g}} + 2M_{\text{fi}} \tag{2.10}$$

where M_{m}, M_{fo}, M_{g} and M_{fi} are masses of mirror, outer flexure, gimbal and inner flexure respectively. Spring constant for the Design B can be calculated by using Eq. (2.8).

2.1.4. Power Amplifier

A 3D printed, photopolymer which is named VeroClear, material based micro-scanner which can be actuated by a varying magnetic field is utilized in the system. Thus, electromagnetic actuation is chosen as the actuation method. In this method, according to the power of the magnetic field, micro-scanner's field of view (area scanned by micro-scanner, FOV) changes. Field of view of the micro-scanner expands with greater magnetic field because movement of micro-scanner is linearly dependent with magnetic field. To create greater magnetic field, current applied to electro-coil should be increased according to Ampere's Law which can be expressed as;

$$B = \mu n I \tag{2.11}$$

where B is the magnetic field strength, μ is the permeability of the core material, n is the turn density of the coil and I is the amplitude of the driving current signal. In respect to (2.11), magnetic field is linearly dependent with permeability, turn density and current. The permeability and turn density values are material dependent; and, they are set by the coil used in the setup.

Displacement values of 3D printed micro-scanners is shown in Figure 2.4. In order to get adequate field of view for micro-scanner of this setup, a minimum driving

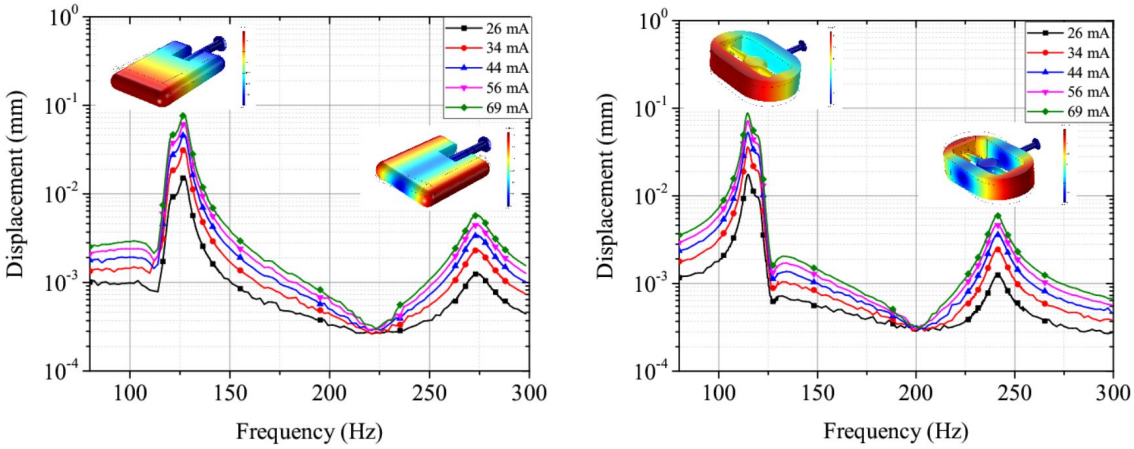

Figure 2.4. Frequency response of micro-scanners for different electrocoil driving current values a) Design A b) Design B [37].

current value of 69 mA should be applied to the electro-coil. A power amplifier circuit is added to the output of the DAQ card, since the maximum output current value of the DAQ Card is measured to be 5 mA which is not sufficient to drive electro-coil. To amplify the output current of the DAQ Card, an amplification circuit with LM 386 power amplifier is added to the setup. LM 386 is used as the amplifier due to its wide range of gain, which can be adjusted between 20 and 200 by connecting a proper resistor between pins 1 and 8. It can operate between 4V-12V DC supply voltage; and it also has low quiescent current consumption which is 4 mA. The power amplifier circuit in Figure 2.5 is designed and utilized in system. In the designed circuit, 12V is used as DC supply. Simulations of the power amplifier circuit is run on Multisim software. Results for AC sweep simulation of the power amplifier circuit is shown in Figure 2.6. In the LSCM system, output of the power amplifier is connected to an electro-coil. In simulations, electro-coil is modeled as an 1mH inductor.

In the simulation result, 309 nW voltage source power is amplified to 1.29 W. According to AC sweep simulation results, designed circuit provide 50 dB gain between 100 Hz and 335 Hz. This frequency range is appropriate for the operation considering resonant frequencies of micro-scanners utilized in the LSCM system. By setting frequency range of the amplifier circuit to these frequency values, undesired high frequency input signals that can trigger unwanted modes of the micro-scanner is

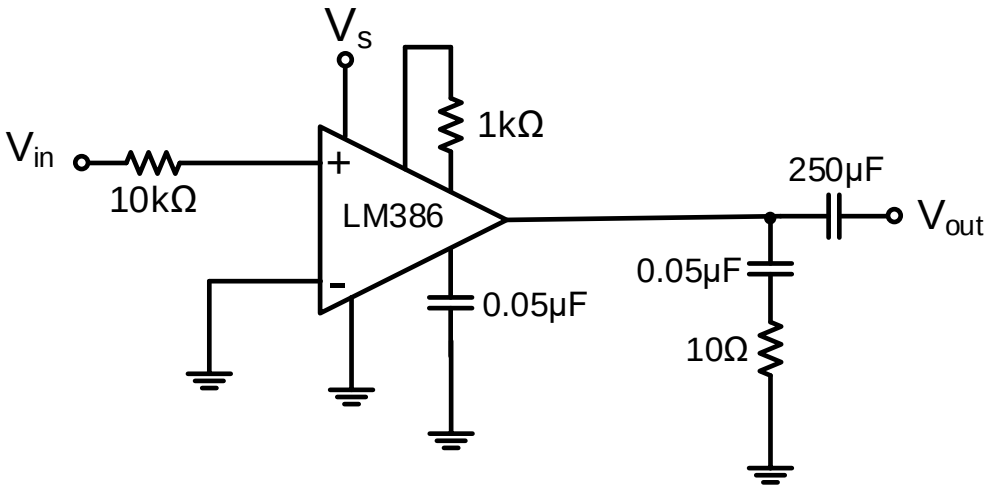

Figure 2.5. Power Amplifier Circuit Schematic.

prevented. Moreover, a Boucherot cell which is composed of 0.05 μF capacitor and 10 Ω resistor is used in the circuit to damp high frequency oscillations and provide stability for the output signal. A DC Block capacitor (250 μF) is used for blocking the DC component of the output signal. The resulting AC signal is coupled to the electro-coil to obtain the desired scanning movement.

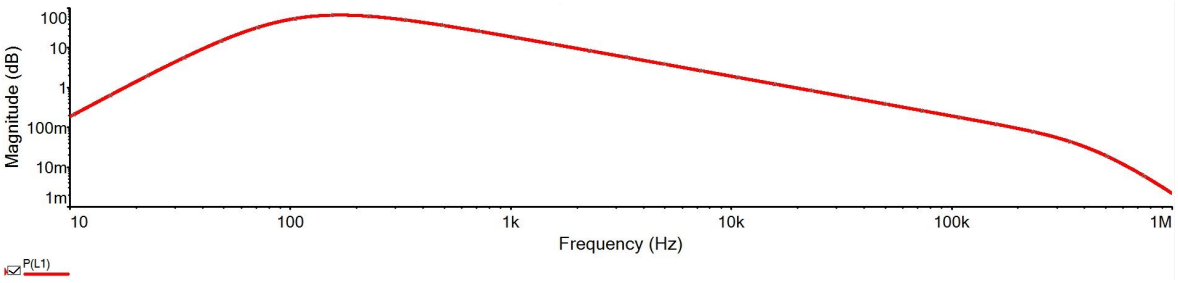

Figure 2.6. AC Sweep Simulation Results for Power Amplifier.

2.1.5. Galvanometer

Galvanometer is a scanning unit which steer laser beams to the target by movement of its mirrors. Galvanometers scan target along vertical and horizontal axes namely slow and fast scan directions. Unlike micro-scanners, galvanometers can be actuated with intended scanning frequencies.Additionally, different waveforms can be

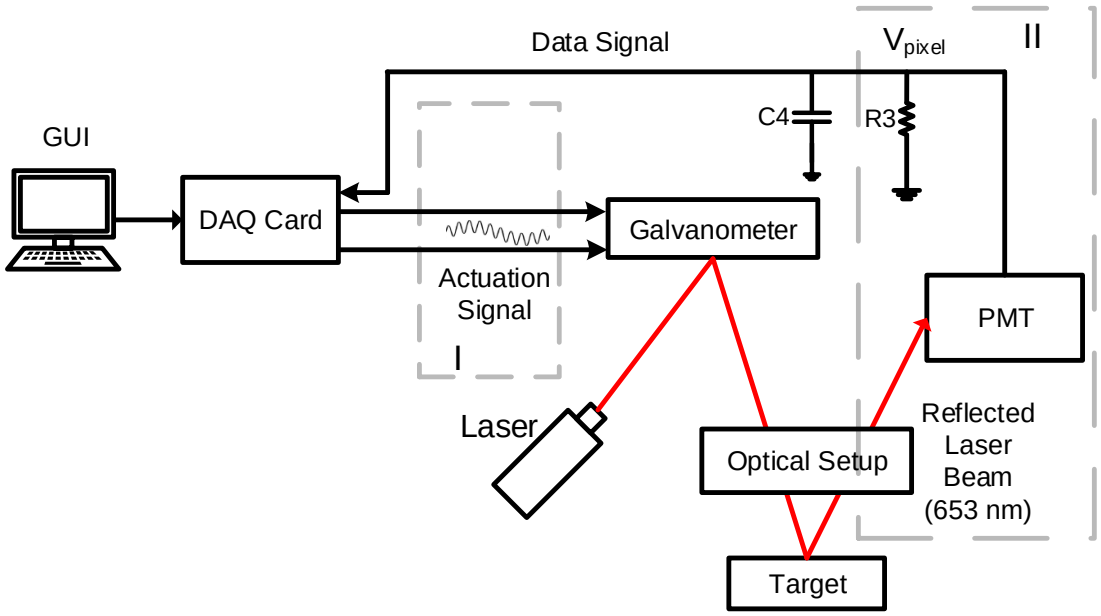

Figure 2.7. Block diagram of the proposed system.

employed to actuate galvanometers. However, frame rates provided by galvanometers are low compared to the micro-scanners.

One of the important components of LSCM systems is utilized scanner and its performance. In the proposed LSCM system, Thorlabs' GVS002/M galvanometer is also utilized as a 2D scanner. Utilized galvanometer's maximum scanning angle is $\pm 12.5°$ and maximum scanning frequency is 250 Hz. The galvanometer provides $1000\mu m \times 1000\mu m$ FOV with implementation of objective lens and relay optic lens to the system.

2.2. Galvanometer Based LSCM System

The block diagram of the proposed system is shown in Figure 2.7. The proposed system is designed to acquire a 2D image from a target by raster-scanning it with the help of a galvanometer. A software controlled DAQ Card is used in the system to simultaneously generate both the actuation signals and the targeted image. To successfully complete the scanning process, galvanometer should make a scanning movement in orthogonal directions namely fast and slow scan directions. Orthogonal movement

of the galvanometer is achieved by applying two separate actuation signals with predefined and precised fast and slow scan frequencies. In this case, to acquire a 2D image from the target, two output channels of the DAQ card should be employed to actuate galvanometer in two orthogonal directions. A function generator software program is formed on MATLAB just to generate such actuation signals. Important specifications of the actuation signals such as amplitude, waveform and frequency could be adjusted from graphical user interface (GUI) of the function generator software. Actuation signals are then physically generated by the DAQ card using these specifications. To control the motion of the galvanometer, these specifications should be adjusted accordingly on the GUI of the program.

The actuated galvanometer scans the target in the direction of slow and fast scan axes by redirecting a laser beam to the target through an optical setup. Laser beam reflected from the target is then gathered by a Photo Multiplier Tube (PMT) after passing through a collection optics. The PMT generates a current based on the intensity of the reflected laser beam. This current value is transformed into a voltage value by simply utilizing a resistor (R3) at the output of the PMT. The voltage value (V_{pixel}) on the resistor R3 is collected by the DAQ card; and is transformed into a pixel intensity value between 0 and 255. This transformation is done in accordance with the calibrated minimum and maximum voltage values. After acquiring the total set of the pixel values in this manner, a 2D image is created and shown on the related GUI. Consequently, both the orthogonal movement of the galvanometer and the construction of the target image can be controlled by MATLAB software. Flowchart of MATLAB program is shown in Figure 2.8.

2.3. Micro-Scanner Based LSCM System

The main target of the proposed system as it is depicted in Figure 2.9 is to basically get a 2D image of a target by Lissajous-scanning it with the help of a micro-scanner. In the proposed system, a DAQ Card controlled by a MATLAB program is utilized both for generating the actuation signal and constructing an image simultaneously.

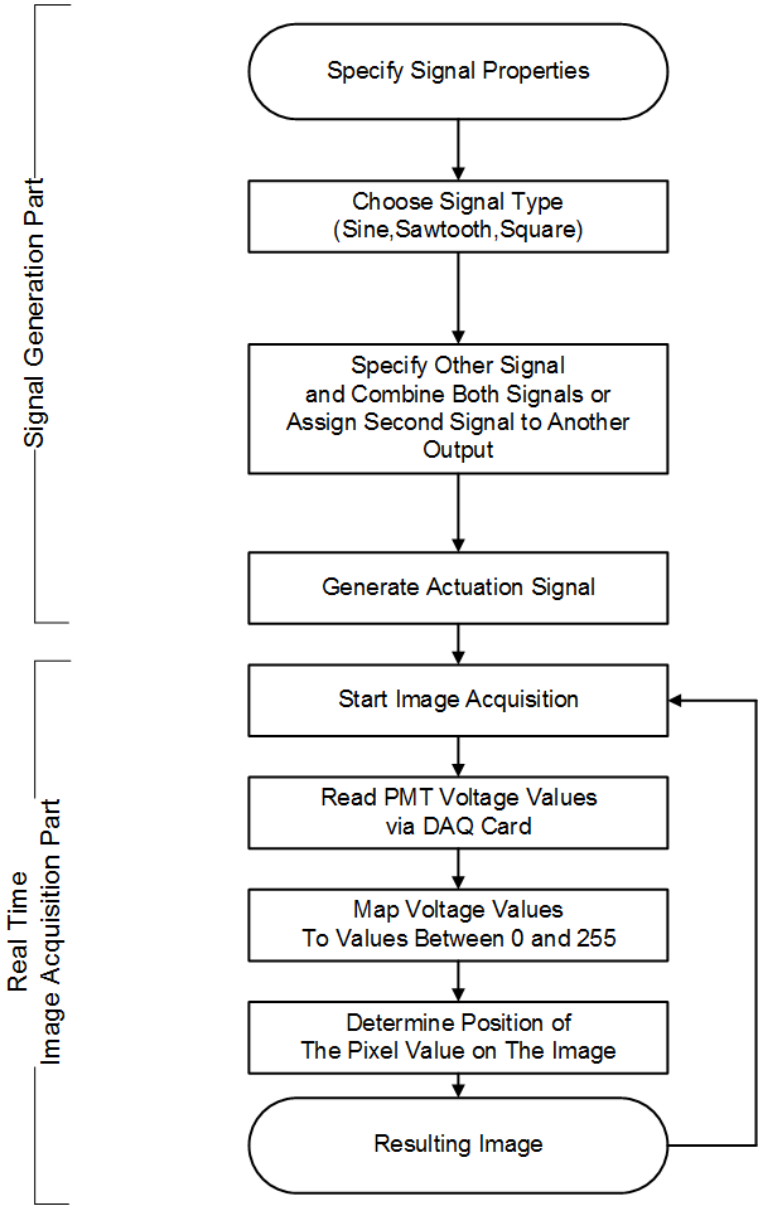

Figure 2.8. Flowchart of the MATLAB program for LSCM.

To accomplish scanning, the micro-scanner should make an orthogonal movement in slow and fast scan directions. The micro-scanner is designed to have some specific fast and slow-scan resonant frequencies which should be precisely triggered. Hence, the actuation signal must contain both slow and fast scan resonant frequencies in order to result in an orthogonal movement. To generate such an actuation signal, a function generator program is written on MATLAB. Waveform, amplitude and frequency of the actuation signal could be defined from graphical user interface (GUI) of the function generator program. The actuation signal is then generated by the DAQ card using these specifications. These specifications can be used to control and adjust the motion

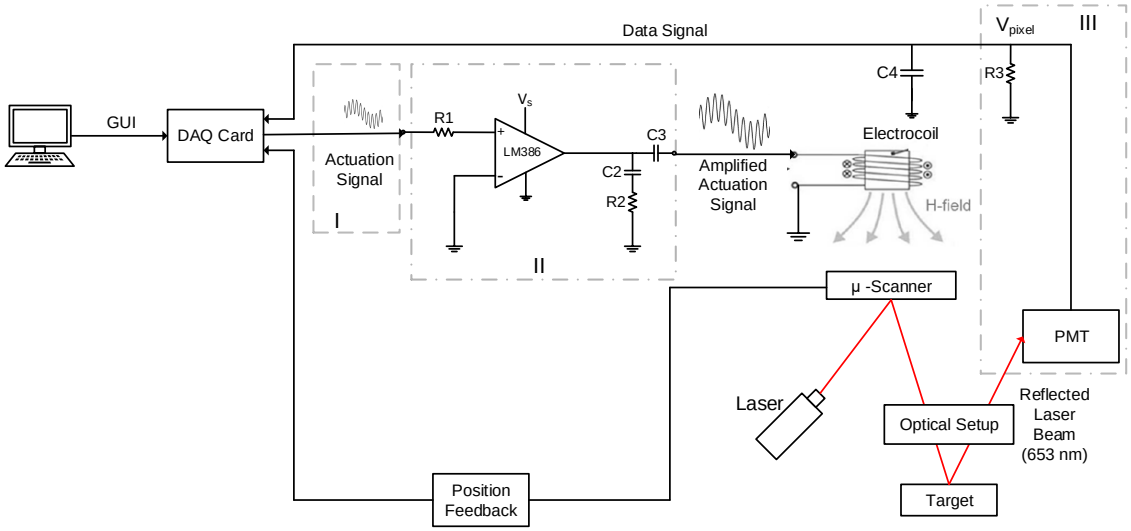

Figure 2.9. Block diagram of the proposed system.

of the micro-scanner. To actuate micro-scanner, besides precise fast and slow scan frequencies, sufficient power should be applied to the micro-scanner for maintaining appropriate field-of-view (FOV). The DAQ Card's maximum output current is 5 mA; and, the maximum output voltage is 10 V. Therefore, it can produce 50 mW maximum power; and, this power does not suffice to obtain an orthogonal scanning movement. Hence, a power amplification circuit is utilized at the analog output channel of the DAQ card. In this circuit LM386 is used as power amplifier. Amplified actuation signal is directed to an electro-coil which will cause actuation of micro-scanner by generating magnetic field.

The actuated micro-scanner scans the target in the direction of fast and slow scan axes by reflecting a laser beam to the target through an optical setup. Laser beam reflected from the target is collected by a PMT after passing through the optical setup. The PMT generates a current depending on to the intensity of reflected laser beam. The current value is converted to voltage value by using a resistor (R3) connected to the output of the PMT. The voltage value (V_{pixel}) on the resistor R3 is acquired by the DAQ Card; and it is converted a pixel intensity value between 0 and 255. This conversion is done according to calibrated maximum and minimum voltage values. After all of the pixel values gathered in this manner, a 2D image is constructed and displayed on the GUI of the MATLAB program. As a result, both actuation of the

micro-scanner and construction of the target image can be controlled on the MATLAB program. Flowchart of the MATLAB program can be seen in Figure 2.8.

3. MICROSCOPE SOFTWARE

The DAQ Card is used to generate actuation signals and acquire voltage values which are converted from output current values of PMT. In order to control DAQ Card, a GUI shown in Figure 3.2 is designed and programmed on MATLAB software. Flowchart of the MATLAB program is shown in Figure 2.8. Firstly, MATLAB program executes signal generation according to the specified signal parameters, and then image acquisition is executed. These two processes are displayed on the GUI as two main blocks; and they are placed on the left and right separately.

3.1. Signal Generation

The left block is the actuation signal generating part, where the right block is the image acquisition/display part. The amplitude, frequency and phase of the actuation signal can be specified on the left block. The actuation signal can be generated in the form of sinusoidal, saw tooth and, square wave as shown in Figure 3.1(a), Figure 3.1(b), Figure 3.1(c), respectively. The actuation signal is created in MATLAB as a matrix by using MATLAB built-in commands. Sampling rate of 3 million samples per second is used for the signal generation; i.e. in order to scan target for 2 seconds, a matrix which is 6000000-by-1 (m-by-n) is created. The matrix is delivered to the DAQ Card's output by using commands in MATLAB Data Acquisition Toolbox.

Actuation signal with one harmonic can be used for actuating the micro-scanner in 1D (along fast scan axis or slow scan axis). To start actuation for micro-scanner in 2D (along both fast scan axis and slow scan axis), two signals with different frequencies must be combined. In combining part of the signal generating left block, the user can combine two different signals and generate an actuation signal with two harmonics to actuate the micro-scanner in 2D. An example 2D actuation signal which contains two sinusoidal signals at 100 Hz and 1 kHz is shown in Figure 3.1(d).In the same manner,

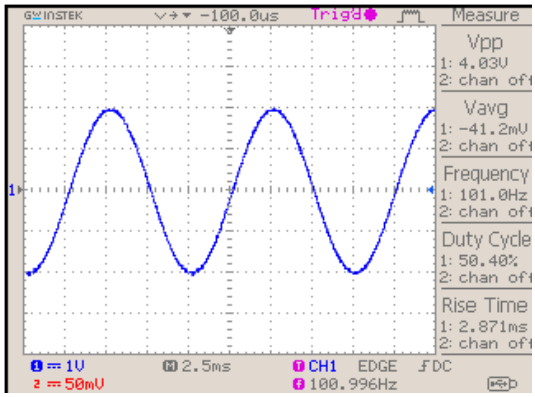

(a) Sinusoidal wave

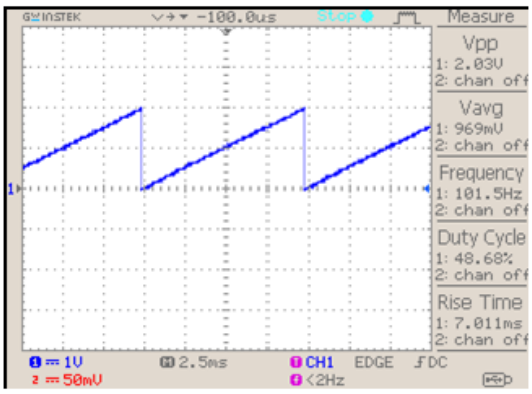

(b) Saw tooth wave

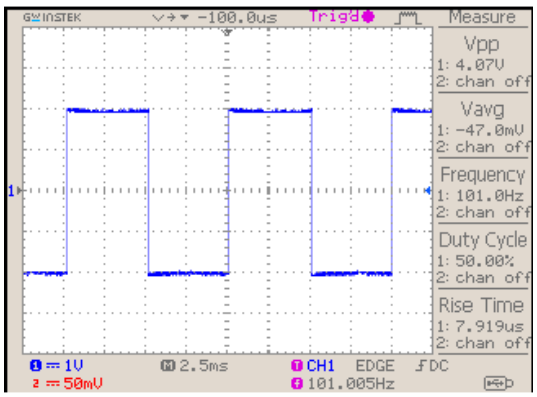

(c) Square wave

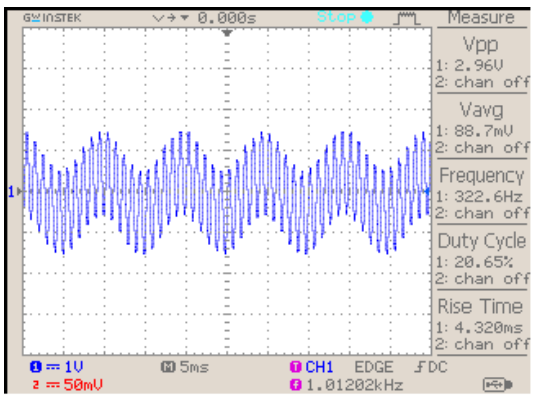

(d) Sine wave with 2 harmonics

Figure 3.1. GUI on MATLAB and example waves generated by DAQ Card with f= 100 Hz and V_{pp}=4. Harmonic wave is composed of 100 Hz and 1 kHz sinusoidal wave.

different types of electromagnetic actuation can be achieved by combining different signal types with specific amplitude, shape, and frequency parameters on the GUI.

In galvanometer case, the signal which is given from one output channel of the DAQ Card can be used to actuate the galvanometer in one dimension along fast or slow scan axis. To start the actuation process in 2D, the user needs to utilize a second output channel. From GUI, separate actuation signals for different channels can be created and can be utilized to start actuation of galvanometer.

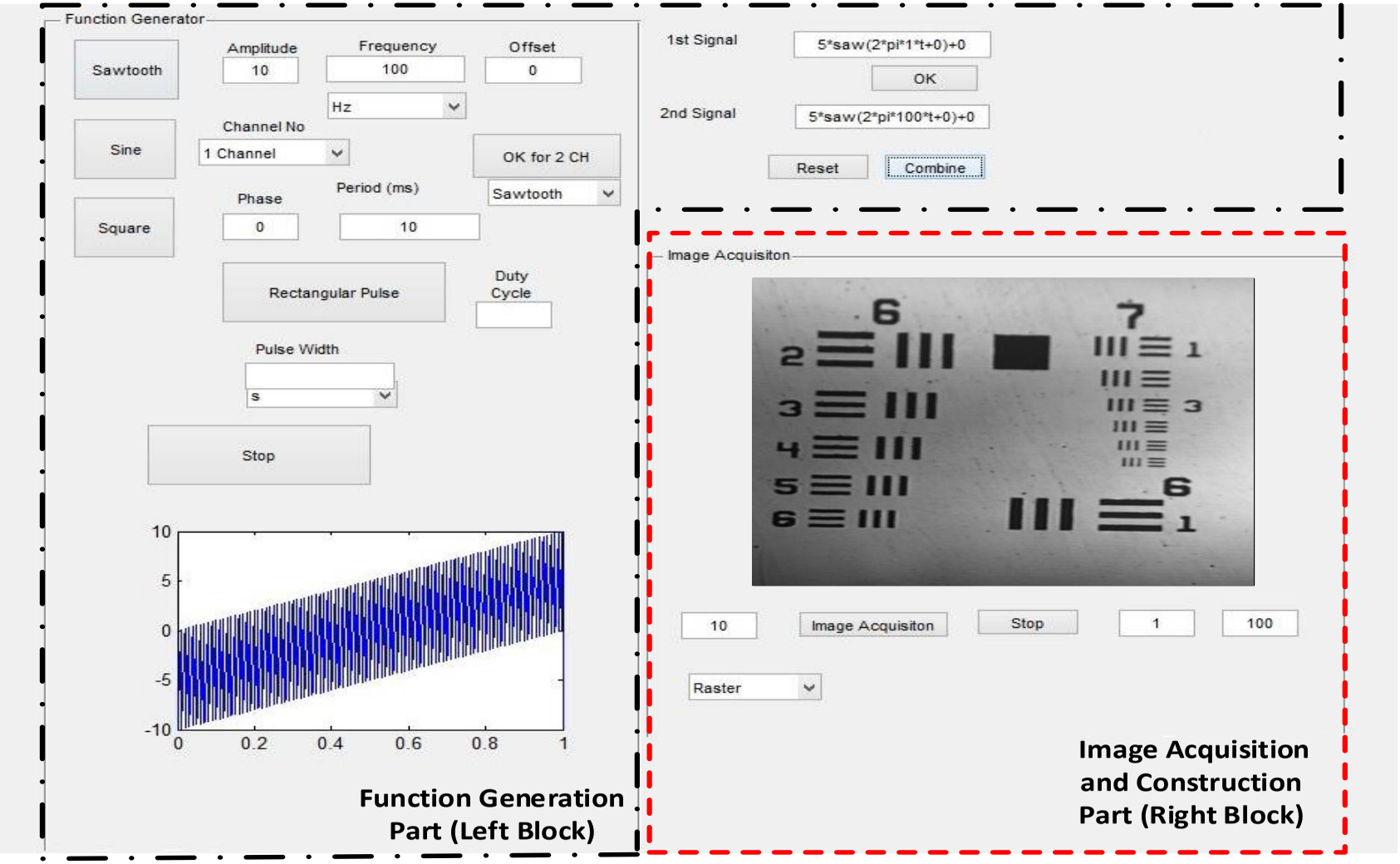

Figure 3.2. GUI on MATLAB.

3.2. Image Acquisition

For the image acquisition and display, the right block of the GUI is allocated. The image constructed using acquired signals is displayed on this block. The user can start data acquisition process by clicking image acquisition button in the right block. When image acquisition process is started, voltage values which are transformed from output current value of PMT by R3 resistor are gathered by DAQ Card in a serial manner through single analog input channel. To designate the pixel value of the gathered voltage value, a calibration method is applied.The incoming voltage value V_{pixel} is transformed to a value between 0 and 255 in the calibration process according to specified maximum and minimum voltage values. In this mapping process, 0 value represents black and 255 represents white color. The transformed value is a pixel for the constructed image. When the image acquisition process is accomplished, the final image is displayed on the GUI.

In the scanning process, two different scanning methods are used. These methods are raster scanning and Lissajous scanning.

3.2.1. Raster Scanning

Raster scanning is capturing an image line by line. Scanning process starts from top-left of the target. After one line is scanned completely, laser beam goes back to beginning of next line. This movement is known as "horizontal retrace". When scanning process for whole target is complete which means that laser beam has reached bottom-right of the target, laser beam goes back to top-left of the target and this movement is known as "vertical retrace". Depicted movement is shown in Figure 3.3.

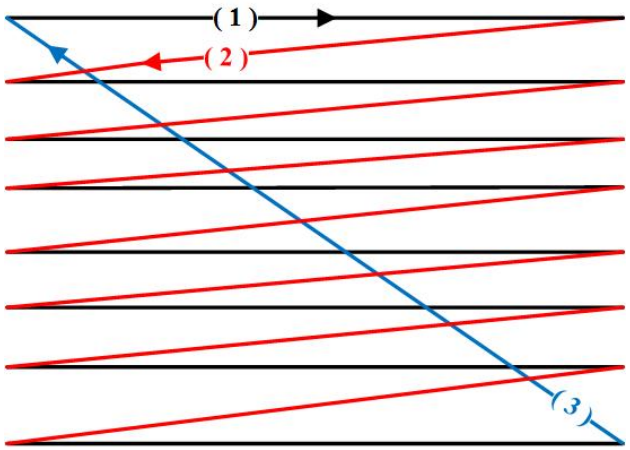

Figure 3.3. Raster Scan Tracing: (1) Scan Line (2) Horizontal Retrace (3) Vertical Retrace.

In real time image acquisition process with raster scanning, the DAQ card generates an actuation signal for one period of slow scan axis actuation signal. This is the time for scanning the whole target only once. This can be stated as;

$$t_{\text{acq}} = \frac{1}{f_{\text{slow}}} \tag{3.1}$$

where, t_{acq} is image acquisition time and f_{slow} is slow scan frequency. The number of rows and number of pixels in a row (number of columns) of the constructed image depend on fast scan frequency, slow scan frequency and sampling rate as;

$$N_{\text{rows}} = \frac{f_{\text{fast}}}{f_{\text{slow}}} \tag{3.2}$$

where, N_{rows} represents number of rows of resulting image, f_{fast} is fast scan frequency and f_{slow} is slow scan frequency. The ratio between fast and slow scan frequencies is

decisive for the number of rows of the constructed image.

$$N_{\text{pixels}} = \frac{f_{\text{s}} t_{\text{acq}}}{N_{\text{rows}}} \tag{3.3}$$

where, N_{pixels} is number of pixels in a row, f_{s} stands for sampling rate, t_{acq} represents image acquisition time and N_{rows} symbolizes number of rows.

In image acquisition with DAQ card and MATLAB, there is delay between actual scanning data and acquired PMT data. When a session is started on DAQ card, DAQ card starts generating driving signals and acquiring values from PMT. However, values generated by PMT are not the actual scanning data until scanning unit of LSCM starts moving. Therefore, some PMT data at the beginning of the process is useless for image reconstruction. If the useless data points are employed in image reconstruction part, they cause distortion at the resulting image. In order to prevent that, the data points which are acquired at the beginning of the process are not employed in image reconstruction process. In experiments, it has been seen that this meaningless data points correspond to %0.01 of the acquired data points.

Additionally, because of barrel distortion, pixels at the edge are not smooth. Therefore, resulting image is cropped nearly %7.5 from left and right side. i.e. assume that galvanometer's slow scan frequency as 1 Hz and fast scan frequency as 100 Hz and sampling rate as 20000 samples per second. In this situation, image acquisition time is 1 second for an image. Number of rows is 100 and number of pixels in a row is 200. In consequence of barrel distortion, resulting image is cropped from %7.5 from left and right side. In the end, 170 x 100 image is displayed on GUI for this scenario.

For the real time display, one period of scanning process is repeated until user decides to stop the process. To decide frame per second (FPS) value of the system

(3.4) can be used.

$$FPS = \frac{1}{t_{\text{acq}} + t_{\text{op}}} \tag{3.4}$$

where t_{acq} is image acquisition time in (3.1) and t_{op} is the process time of the MATLAB program. In the experiments, image display time ($t_{\text{acq}} + t_{\text{op}}$) values were nearly 2 seconds. Therefore, FPS value of the system is nearly 0.5. Raster scanning algorithm is shown in Figure 3.4

Require V_{pixel} values with length L, mapped between 0 and 255
Add delay with length D to the end of V_{pixel} values;
Take V_{pixel} values from D to $L + D$;
Compute t_{acq} using Eq. 3.1;
Compute N_{rows} using Eq. 3.2;
Compute N_{pixels} using Eq. 3.3;
for $i = 1$ to N_{rows} **do**
  $I(i,:) = V_{\text{pixel}}((i-1)(N_{\text{pixels}}) + 1 : (i)(N_{\text{pixels}}))$;
end for

Figure 3.4. Raster Scanning Algorithm.

3.2.2. Lissajous Scanning

In the designed LSCM system, 3D printed micro-scanners are utilized as scanning unit.When micro-scanners are utilized, to reconstruct a meaningful image of a target, Lissajous scanning is employed because in raster scanning resolution of acquired image depends on proportion of fast and slow scan frequencies and with micro-scanner the ratio between fast and slow scan frequencies could be very low. Therefore, acquiring a meaningful image could be prevented. Lissajous scanning patterns are often employed in laser scanning systems where the more common raster scanning pattern is impractical. This is often the case in miniaturized laser scanning microscopes using MEMS scanning mirrors or piezoelectric fiber scanners for beam scanning [4,5,15,39–41]. Reason of that is with appropriate scanning frequencies desired FOV can be scanned completely by Lissajous patterns. Usage of Lissajous scanning has led up to rapid imaging

in atomic force microscopy and multiphoton microscopy [4, 42]. Coupled with image interpolation algorithms, 2D Lissajous scanning provides frame rate above 1 kHz [43].

In mathematics, a Lissajous curve is the graph of a system of parametric equations (3.5) and (3.6)

$$x(t) = X \sin(2\pi f_{\mathrm{x}} t + \phi_{\mathrm{x}}) \tag{3.5}$$

$$y(t) = Y \sin(2\pi f_{\mathrm{y}} t + \phi_{\mathrm{y}}) \tag{3.6}$$

which describe complex harmonic motion. Here f_{x} and f_{y} are driving frequencies in the x and y directions while ϕ_{x} and ϕ_{y} are phase shifts. X and Y are maximum values $x(t)$ and $y(t)$ could get. In other words, X and Y represent borders for field of view (FOV) in x and y directions respectively.

The figure which is constituted from these equations is highly sensitive to the ratio $\frac{f_{\mathrm{x}}}{f_{\mathrm{y}}}$. Number of lobes of the figure is determined by the ratio $\frac{f_{\mathrm{x}}}{f_{\mathrm{y}}}$. For example, a ratio of 2/1 produces a figure with two major lobes. In the same manner a ratio of 4/3 creates a figure with four horizontal lobes and three vertical lobes. Examples can be seen in Figure 3.5.

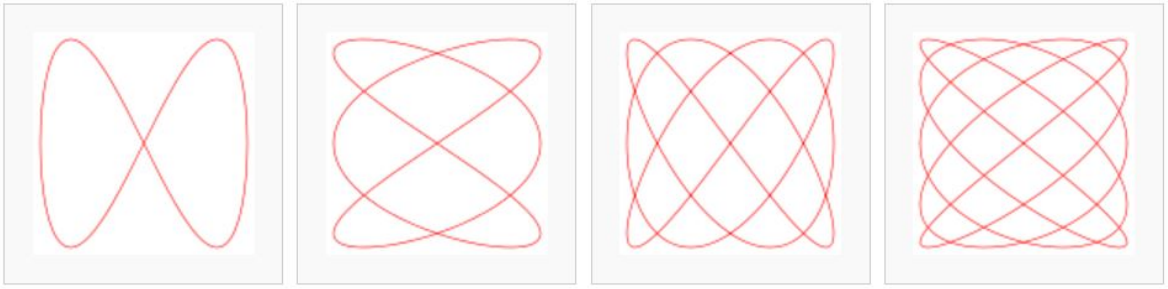

Figure 3.5. Lissajous Curves Examples for $\frac{1}{2}, \frac{3}{2}, \frac{3}{4} and \frac{5}{4}$ values of $\frac{f_{\mathrm{x}}}{f_{\mathrm{y}}}$ from Left to Right [47].

While constructing an image from data which is acquired with Lissajous scan, points which are results of (3.5) and (3.6) is used as pixel locations. Each data must be placed in corresponding $(y(t_{\mathrm{n}}), x(t_{\mathrm{n}}))$ position in the image matrix. Here $(y(t_{\mathrm{n}})$ and $(x(t_{\mathrm{n}})$ are row number and column number for n^{th} data respectively. However, it is known that row and column numbers of a matrix must be positive integers. To ensure this condition, a series of processes must be applied to (3.5) and (3.6).

As a beginning, (3.5) and (3.6) must be changed as:

$$x(t) = \frac{1}{2}X[\sin(2\pi f_{\mathrm{x}}t + \phi_{\mathrm{x}}) + 1] \tag{3.7}$$

$$y(t) = \frac{1}{2}Y[\sin(2\pi f_{\mathrm{y}}t + \phi_{\mathrm{y}}) + 1] \tag{3.8}$$

As a result of (3.7) and (3.8), $x(t)$ and $y(t)$ values become such that $0 \leqslant x(t) \leqslant X$, $0 \leqslant y(t) \leqslant Y$.

Resolution of the constructed image depends on numerical aperture (NA) of objective lens and wavelength of the utilized laser in the system. Width and height of the constructed image must be scaled according to lateral full-width-half-maximum (FWHM) resolution value which can be expressed as [48];

$$w_r = \frac{2\sqrt{\ln 2}\ 0.32\ \lambda}{NA} \tag{3.9}$$

where NA is numerical aperture of the lens and λ is wavelength of the utilized laser. To specify width and height of the image, X and Y values are divided with the lateral

FWHM resolution w_r. Image width and image height can be expressed as;

$$I_{\mathrm{w}} = \frac{X}{w_r} \tag{3.10}$$

$$I_{\mathrm{h}} = \frac{Y}{w_r} \tag{3.11}$$

where I_{w} and I_{h} represent image width and height respectively. To assign position data $x(t)$ and $y(t)$ values between 0 and I_{w} or I_{h}, they are also divided with the lateral FWHM resolution w_r.

$$x(t)_{\mathrm{s}} = \frac{x(t)}{w_r} \tag{3.12}$$

$$y(t)_{\mathrm{s}} = \frac{y(t)}{w_r} \tag{3.13}$$

where $x(t)_{\mathrm{s}}$ and $y(t)_{\mathrm{s}}$ are scaled versions of $x(t)$ and $y(t)$ respectively. As a result of the process $x(t)_{\mathrm{s}}$ and $y(t)_{\mathrm{s}}$ are such that $0 \leqslant x(t)_{\mathrm{s}} \leqslant I_{\mathrm{w}}$, $0 \leqslant y(t)_{\mathrm{s}} \leqslant I_{\mathrm{h}}$. In MATLAB, matrix indexes start from one. As a result of that, to eliminate all zero values in $\mathrm{x(t)_s}$ and $\mathrm{y(t)_s}$, 1 is added to them and then they are rounded because $\mathrm{x(t)_s}$ and $\mathrm{y(t)_s}$ is used as matrix indexes therefore they must be positive integers.

Elements of scanning data are placed in matrix according to corresponding row and column index values $\mathrm{x(t)_s}$ and $\mathrm{y(t)_s}$. In the end, image is constructed. However, in image acquisition with DAQ card and MATLAB, there is delay between actual scanning data and acquired PMT data. When a session is started on DAQ card, DAQ card starts generating driving signals and acquiring values from PMT. However, values

generated by PMT are not the actual scanning data until scanning unit of LSCM starts moving. Therefore, some PMT data at the beginning of the process is useless for image reconstruction. If the useless data points are employed in image reconstruction part, they cause distortion at the resulting image. In order to prevent that, the data points which are acquired at the beginning of the process are not employed in image reconstruction process. In experiments, it has been seen that this meaningless data points correspond to %0.01 of the acquired data points.

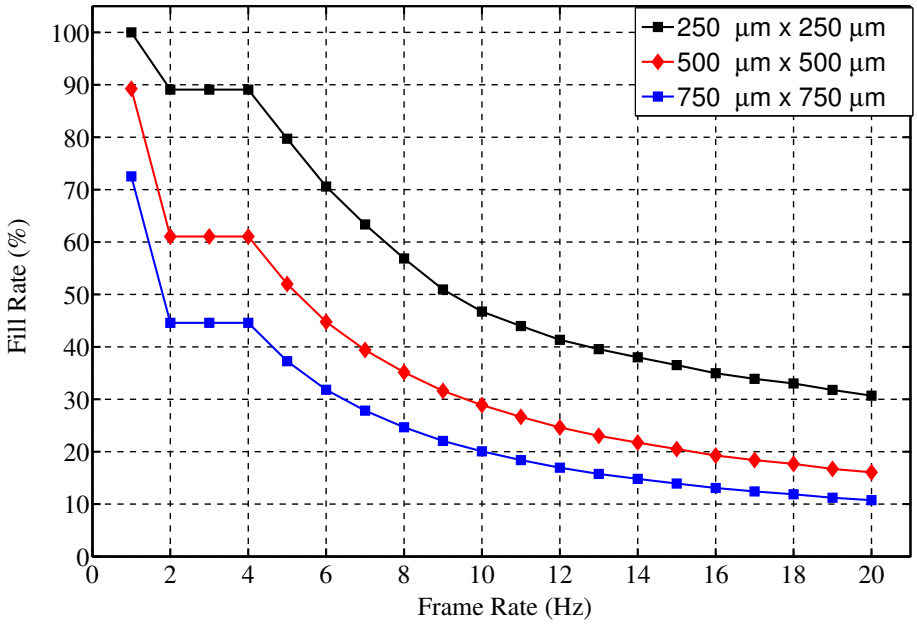

Figure 3.6. Fill Rates of Lissajous Scanning for Different FOV Values.

As mentioned before, the figure which is formed by Lissajous patterns highly depends on the ratio $\frac{f_x}{f_y}$. For a selected spot size and FOV, Lissajous scan coverage rate increases with mutually prime scanning frequencies. Coverage rate of Lissajous scan also increases when frame rate of the system is decreased. Comparison between different frame rates and scanning frequencies is shown in Figure 3.9 In addition to that, fill rate of a Lissajous scan at different frame rates for different FOV values is presented in Figure 3.6. Maximum fill rates for different frame rate values are provided in Figure 3.7. Additionally, frequency pairs that provide the maximum fill rates for different frame rates are presented in Table 3.1. There are 11384 different frequency pairs which can scan whole are for 1 Hz frame rate value. Therefore, just one example among the frequency pairs is provided in Table 3.1 for 1 Hz frame rate. In the table,

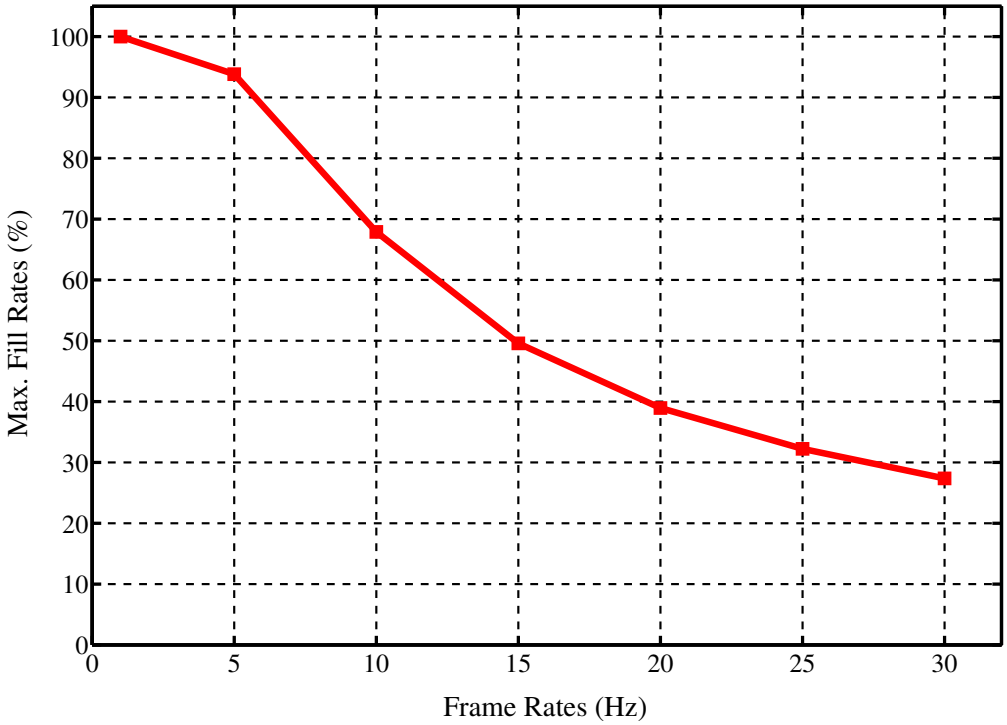

Figure 3.7. Maximum Fill Rates of Lissajous Scanning for Different Frame Rates.

frequency pairs are presented as f_x and f_y values respectively. However, f_x and f_y values can be swapped. Swapping f_x and f_y values does not affect the maximum fill rate value for corresponding frame rate. Lissajous scanning algorithm is shown in Figure 3.8.

Table 3.1. Maximum Fill Rates for Different Frame Rates and Frequency Pairs that Provide the Maximum Fill Rate Values.

Frame Rate (Hz)	**Max. Fill Rate (%)**	**Frequency Pair (f_x & f_y)**
1	100	100 Hz & 101 Hz
5	93.82	288 Hz & 291 Hz
10	67.89	298 Hz & 300 Hz
15	49.56	298 Hz & 300 Hz
20	38.94	288 Hz & 299 Hz
25	32.23	287 Hz & 300 Hz
30	27.37	287 Hz & 300 Hz

Require V_{pixel} values with length L, mapped between 0 and 255
Add delay with length D to the end of V_{pixel} values;
Compute the FWHM using Eq. 3.9;
Compute scaled position data $x(t)_s$ and $y(t)_s$ using Eq. 3.7, 3.8, 3.12, 3.13;
Add 1 to $x(t)_s$ and $y(t)_s$;
for $i = D$ to $L + D$ **do**
  $I(y_s(i), x_s(i)) = V_{pixel}(i)$;
end for

Figure 3.8. Lissajous Scanning Algorithm.

3.3. Noise Reduction

An image generally is exposed to noise in its reconstruction or transmission process. Aim of denoising process is to separate noise from image and remove it without doing any harm to original image. Image filtering by using wavelet transform is one of the methods to do this task. Wavelet transform is useful for image filtering applications because it conserves energy in transformation and inverse transformation steps. By thresholding image coefficients which is acquired by using wavelet transform intended filtering process can be done [49]. Under the assumption of characteristic of image noise is additive white Gaussian noise, it can be seen that coefficients are also affected in the same way [50]. For the method of thresholding besides non-linear method which is proposed by Donoho and Johnstone, there are plenty of other methods in literature [51–54]. All of these methods are used in signal processing and image processing applications.

Applied filter method can be summarized in three steps. Firstly, Discrete Wavelet Transform (DWT) is applied and coefficients are acquired by transforming discrete data from time domain to time-frequency domain. While numerically lesser coefficients are affected by noise greatly, numerically greater coefficients carry more information about

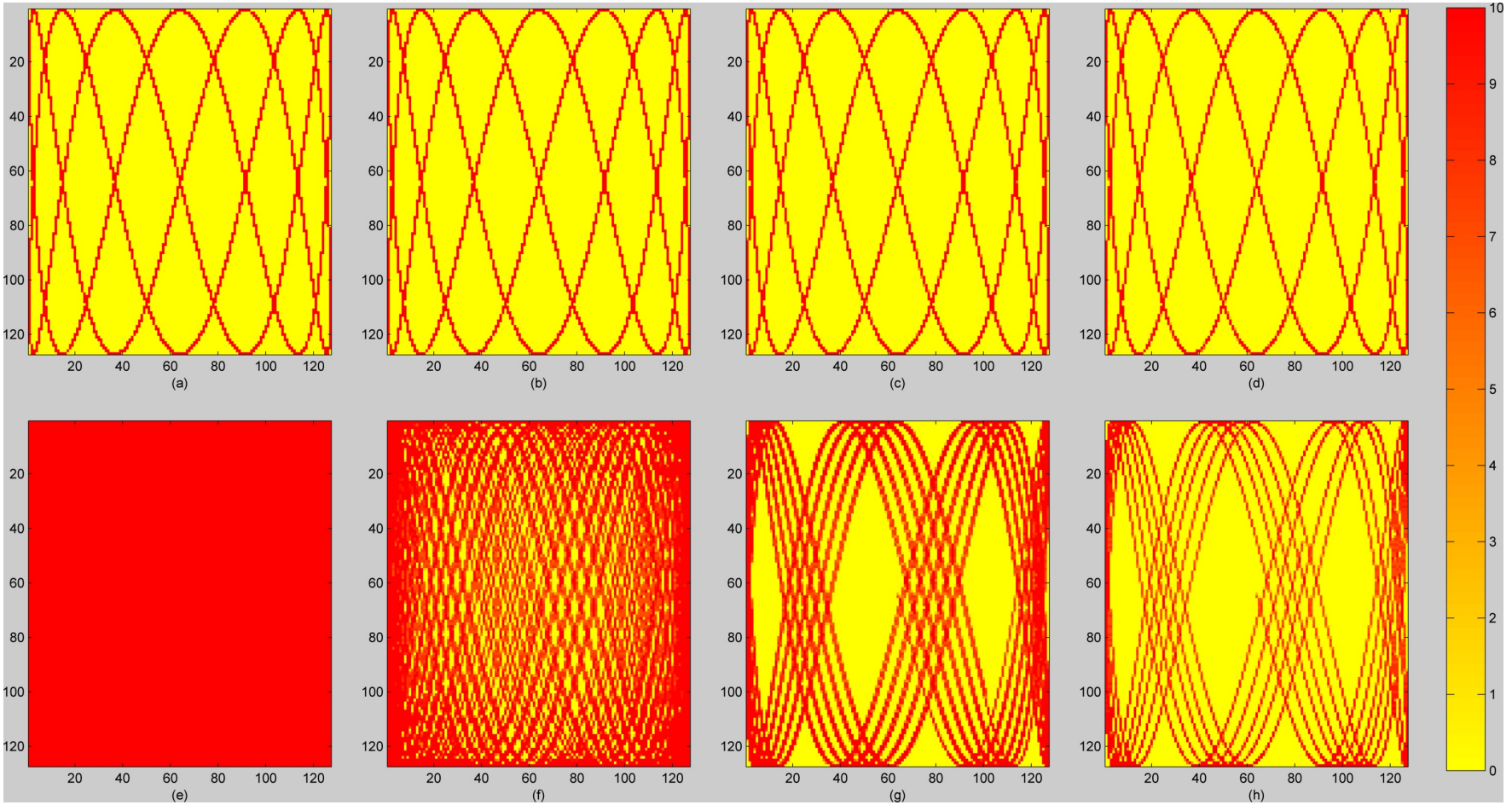

Figure 3.9. Lissajous patterns for various scan frequencies and frame rates. Horizontal and vertical frequencies for (a)-(d) and (e)-(h) are $f_x = 100$ Hz, $f_y = 350$ Hz and $f_x = 101$ Hz, $f_y = 351$ Hz respectively. Frame rates from (a) to (d) and from (e) to (h) are 1, 5, 10 and 20 Hz. Fill rates for (a)-(d) are %13.4 and from (e) to (h) are %30.7, %46.7, %79.7 and %100, respectively.

original image. Secondly, thresholding is applied to wavelet coefficients. Thresholding eliminates non-linear wavelet transformation coefficients assuming that these coefficients are components of noise. These coefficients are set to zero [55]. Coefficients which are greater than threshold are either left untouched or shrunk by the amount of the threshold value. These thresholding processes are called hard thresholding and soft thresholding respectively. Finally, inverse transform is applied to data values which are above threshold. Selection of the threshold value is highly important because threshold values which are far lesser from optimum threshold value cause less denoising on image, threshold values which are far greater from optimum threshold value cause elimination of important data. Elimination of important data can cause smoothing or falsification on the original data. [56, 57]. In this thesis, effectiveness of the wavelet transformation on image denoising tested on MATLAB environment. To compare different thresholding techniques Peak Signal to Noise Ratio (PSNR) concept is used. The most effective method is applied to images which are acquired from laser scanning confocal microscopy system. Results are presented in Experiments and Results part.

3.3.1. Discrete Wavelet Transform

As shown in [56], the mathematical approach to the discrete wavelet transform (DWT) is based on the fact that a function $f(t)$ can be linearly expressed as:

$$f(t) = \sum_{k} a_{\mathrm{k}} \psi_{\mathrm{k}}(t) \tag{3.14}$$

where a_k are the analysis coefficients and ψ_{k} are the analyzing functions, which are named as basis functions if the analysis in Eq. 3.14 is unique. If the basis functions are orthogonal, relationship between them expressed as:

$$\langle \psi_{\mathrm{k}}(t), \psi_{\mathrm{l}}(t) \rangle = \int_{0}^{x} \psi_{\mathrm{k}}(t) \psi_{\mathrm{l}}(t)\, dt = 0 \quad for \quad k \neq l \tag{3.15}$$

the analysis coefficients can be calculated by using following equation:

$$a_k = \langle f(t), \psi_{\mathrm{k}}(t) \rangle = \int_0^x f(t)\psi_{\mathrm{k}}(t)\, dt \tag{3.16}$$

For example, in Fourier transform, the orthogonal analysis functions are sinus and cosinus. Generally, 2D signal can be transformed by DWT as:

$$f(t) = \sum_k \sum_j a_{\mathrm{j,\,k}} \psi_{\mathrm{j,\,k}}(t) \tag{3.17}$$

where $a_{\mathrm{j,\,k}}$ are the transform coefficients and $\psi_{\mathrm{j,\,k}}$ are the basis functions. If $a_{\mathrm{j,\,k}}$ and $\psi_{\mathrm{j,\,k}}$ are known, Eq. 3.17 is the inverse transform. Hence, a function $f(t)$ can be represented by transform coefficients, which are obtained from internal product of that function with an orthogonal basis function. On the other hand, the function can be reconstructed from these coefficients and the basis function. Wavelets are these basis functions. [58–60]

Another usage of wavelets is the subband coding theory or multiresolution analysis [61]. The signal passes consecutively through analysis filters which are pairs of low pass and high pass filters. As a result of that process, the transform coefficients are produced. If the transform coefficients can pass through synthesis filters consecutively, initial signal can be reconstructed. The most basic property of the analysis and synthesis filters is orthogonal relationship between them because produced coefficients must preserve the energy of the initial signal. In Figure 3.10, analysis of a 1D signal with the subband coding theory which is identical to wavelet decomposition is shown [56].

The high pass filters represent high frequency components or in another saying details of signal and the low pass filters represent approximation of the signal or in another saying DC component of the signal. Wavelet decomposition is the successive analysis of only the low pass component. It is shown in Figure 3.10(b). The analysis

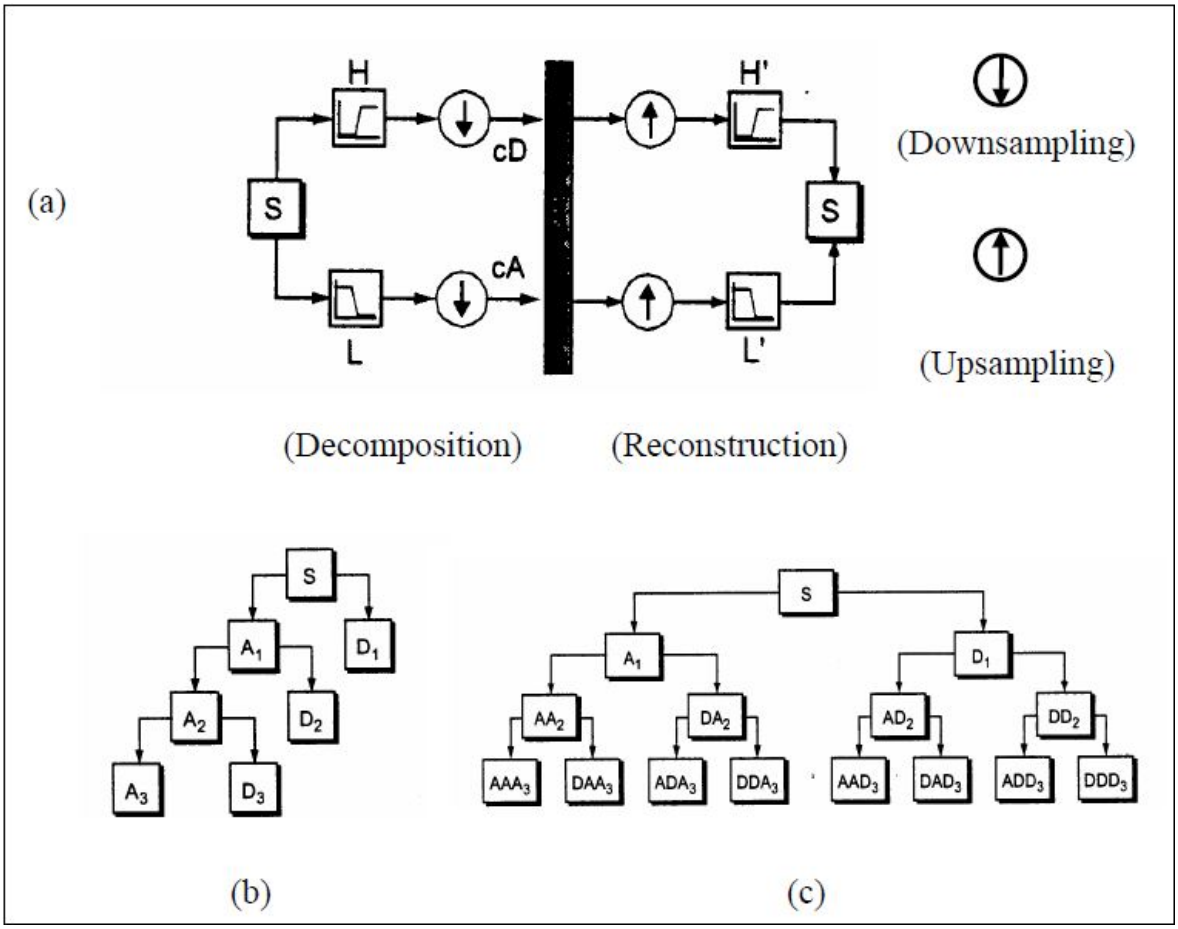

Figure 3.10. Analysis and synthesis of a 1D signal with subband coding. (a) DWT and Inverse DWT of 1D signal, (b)DWT tree, (c)Wavelet packet tree

of both low and high pass components is called wavelet packet decomposition. It is shown in Figure 3.10(c). The input signal S in Figure 3.10 can be written as:

$$S = A_3 + D_3 + D_2 + D_1 \quad or \quad S = A_2 + D_2 + D_1 \quad or \quad S = A_1 + D_1 \tag{3.18}$$

Likewise, by using wavelet package decomposition, the input signal can be written as:

$$S = A_1 + AAD_3 + DAD_3 + ADD_3 + DDD_3 \tag{3.19}$$

The decomposition tree is called as wavelet tree. Along with its coefficients, it is also transferred to the decoder for reconstruction of the initial signal.

The wavelet transform is very useful for image handling because of its beneficial features. These features can be listed as:

- It can compact most of the signal's energy into a few transformation coefficients. This is called as energy compaction.
- It can effectively capture and represent high and low frequency components of an image.
- The variable resolution decomposition with almost uncorrelated coefficients.
- The ability of a progressive transmission, which facilitates the reception of an image at different qualities.

In that case, presence of small coefficients is more likely because of the noise contamination, while the large coefficients contain important details of image. Therefore, small coefficients can be thresholded without touching large coefficients. Therefore, image quality can be increased. Thresholding techniques which are plain non-linear techniques, eliminate subband coefficients which have magnitude less than threshold value. The two mostly used methods of thresholding are soft thresholding and hard thresholding [62]. In hard thresholding, the coefficients below threshold are eliminated, those which are above threshold stays same. However, in soft thresholding, coefficients which are above threshold also changes. They shrunk at the amount of the threshold value. Coefficients below threshold are eliminated in the same manner with hard thresholding.

In Figure 3.11, two level DWT of a 2D signal is shown which includes subbands LL_2(low frequency coefficients), HL_2 (horizontal details), LH_2 (vertical details), HH_2 (diagonal details) and the first level details HL_1, LH_1, HH_1 [58].

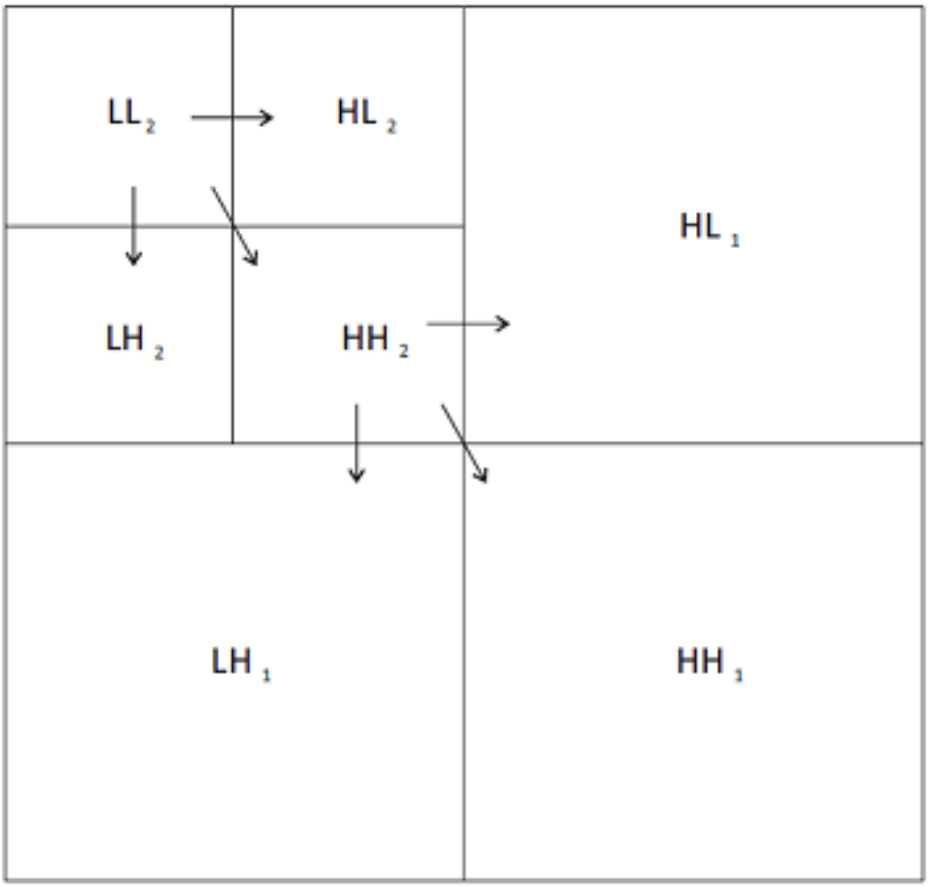

Figure 3.11. Two level Discrete Wavelet Transform

3.3.2. Thresholding Method and Selection of the Threshold Value

Suppose $\{x_{\mathrm{i,\,j}}, 1 \leq i, j \leq n, m\}$ is an image of $P = n \times m$ pixels, which is corrupted by white Gaussian noise, then the model for the noisy image can be expressed as:

$$y_{\mathrm{i,\,j}} = x_{\mathrm{i,\,j}} + \epsilon_{\mathrm{i,\,j}}, \qquad 1 \leq i, j \leq n, m \tag{3.20}$$

where $y_{\mathrm{i,\,j}}$ is noisy image and $\epsilon_{\mathrm{i,\,j}}$ is independent and identically distributed (i.i.d), zero mean white Gaussian noise with standard deviation σ. The noise can be denoted as $\epsilon_{\mathrm{i,\,j}} \sim N(0, \sigma^2)$. Aim of the denoising process is to estimate image x from noisy image y, such that Mean Square Error (MSE) to be minimum. The MSE can be calculated

by using Eq. 3.21.

$$MSE = \frac{1}{P}\|\hat{x} - x\|^2 = \frac{1}{P}\sum_{i,j}^{P=n\times m}(\hat{x}_{\mathrm{i,\,j}} - x_{\mathrm{i,\,j}})^2 \tag{3.21}$$

where $\hat{x}$ is estimation of original image x from noisy image y. Estimation procedure involves three steps.

Firstly, 2D DWT is applied to noisy image y to obtain subband approximate coefficients, horizontal details, vertical details and diagonal details. Assume that W and W^{-1} represent 2D DWT and its inverse respectively. Therefore, original image, noisy image and noise have a matrix form which are shown in Eq. 3.22 in transform domain

$$Y_t = Wy, \quad X_t = Wx, \quad N_t = W\epsilon \tag{3.22}$$

Therefore, Eq. 3.20 in spatial domain becomes Eq. 3.23 in transform domain.

$$Y_t = X_t + N_t \tag{3.23}$$

where Y_t, X_t and N_t are transform domains of noisy image, original image and noise respectively. In view of the orthogonal property of the transform, noise in transform domain is also of Gaussian nature.

Secondly, the detail coefficients are thresholded either using hard thresholding (keep or kill rule) or soft thresholding (shrink or kill rule). For a given threshold value δ, expressions of hard and soft thresholding rules can be seen in Eq. 3.24 and Eq. 3.25

respectively.

$$\eta^{\mathrm{H}}(w,\delta) = wI(|w| > \delta) \tag{3.24}$$

$$\eta^{\mathrm{S}}(w,\delta) = sign(w)(|w| - \delta)I(|w| > \delta) \tag{3.25}$$

where w represents transformation coefficients and $I(.)$ is a function which shows coefficients greater than threshold value δ. The thresholded wavelet coefficients are obtained by applying any of the threshold rules above.

Finally, image is reconstructed by applying inverse DWT on the thresholded wavelet coefficients. This process can be expressed as:

$$\hat{x} = W^{-1}\ \widehat{Y} \tag{3.26}$$

where $\widehat{Y}$ is thresholded wavelet coefficients and $\hat{x}$ is reconstructed image which is denoised estimate of x.

The threshold level is estimated by various methods called thresholding criteria which are based on the minimization of the averaged squared error

$$\mathrm{argmin}(\frac{1}{P}\sum_{i}(\widehat{Y}_i - X_i)^2) \tag{3.27}$$

where X_i and $\widehat{Y}_i$ are all the detail subbands' coefficients of the original image and the noised image after thresholding respectively. Additionally, to determine the threshold value, there are other methods such as universal threshold [49] and Stein's Unbiased

Risk Estimate (SURE) threshold [63, 64].

Universal threshold is the optimal threshold in the asymptotic sense and minimizes the cost function of the difference between the function and the soft thresholded version of the same in the L_2 norm sense. Universal threshold can be expressed as:

$$\delta = \hat{\sigma}\sqrt{2\log P} \tag{3.28}$$

where P is the signal length and $\hat{\sigma}^2$ is the noise variance.

Assume that $w_1, w_2, ..., w_P$ are multivariate normal observations which are i.i.d. Gaussian as $N(\mu_i, 1)$ with mean vector $\mu = (\mu_1, ..., \mu_P)^T$. Let $\hat{\mu}$ be a fixed estimate of μ based on the observations. SURE is a method for estimating the loss $||\hat{\mu} - \mu||^2$ in an unbiased fashion.

$$SURE(w, \delta) = P - 2\ \#\{i : |w_{\mathrm{i}}| \leq \delta\} + \sum_{i=1}^{P}[\min(|w_{\mathrm{i}}|, \delta)]^2 \tag{3.29}$$

In Eq. 3.29, #(.) shows cardinality of the set. For an observed vector w, to find the threshold δ^S that minimizes $SURE(w, \delta)$, Eq. 3.30 is applied.

$$\delta^{\mathrm{S}} = \underset{\delta}{\mathrm{argmin}}(SURE(w, \delta)) \tag{3.30}$$

For image denoising, firstly the wavelet decomposition of the noisy image is obtained. Afterwards the SURE threshold is determined for each subband using Eq. 3.29 and Eq. 3.30. In all the above cases, the noise standard deviation can be estimated by using the robust median estimator [51]:

$$\hat{\sigma} = \frac{median(|Y_{\mathrm{i,\,j}}|)}{0.6745} \tag{3.31}$$

While estimating standard deviation of the noise, three different scenarios is applied [56].

First case is global median estimator (GME). In global median estimator case $Y_{\mathrm{i,\,j}}$ in Eq. 3.31 represents the coefficients of HH_1 subband. In second case which is level dependent median estimator (LDME), the same median estimator is used in order to determine the standard deviation of noise for each level separately. In this case, $Y_{\mathrm{i,\,j}}$ represents all the detail coefficients of the corresponding level (i.e. coefficients of the horizontal, vertical and diagonal subbands). In third and final case which is detail dependent median estimator (DDME), the same median estimator is applied on the horizontal, vertical and diagonal detail coefficients of each level. In DDME case, $Y_{\mathrm{i,\,j}}$ represents the corresponding detail coefficients of each level.Results of denoising methods are provided in Experiments and Results chapter.

4. EXPERIMENTAL RESULTS

In this part of the thesis, acquired images from designed LSCM system in real time and results of denoising process are presented.

4.1. Acquired Images From LSCM System

In the conducted tests of the system which can be seen in Figure 4.1, it has been seen that maximum resolution of images which are acquired by utilizing galvanometer can be under 1 μm both in horizontal and vertical axis. Additionally, maximum FOV is calculated as $1000 \times 1000\ \mu m^2$. The values can be adjusted according to desired resolution and FOV. While horizontal resolution depends on sampling rate of the DAQ card, vertical resolution depends on ratio between fast and slow scan frequencies and the ratio depends on specifications of scanning unit.

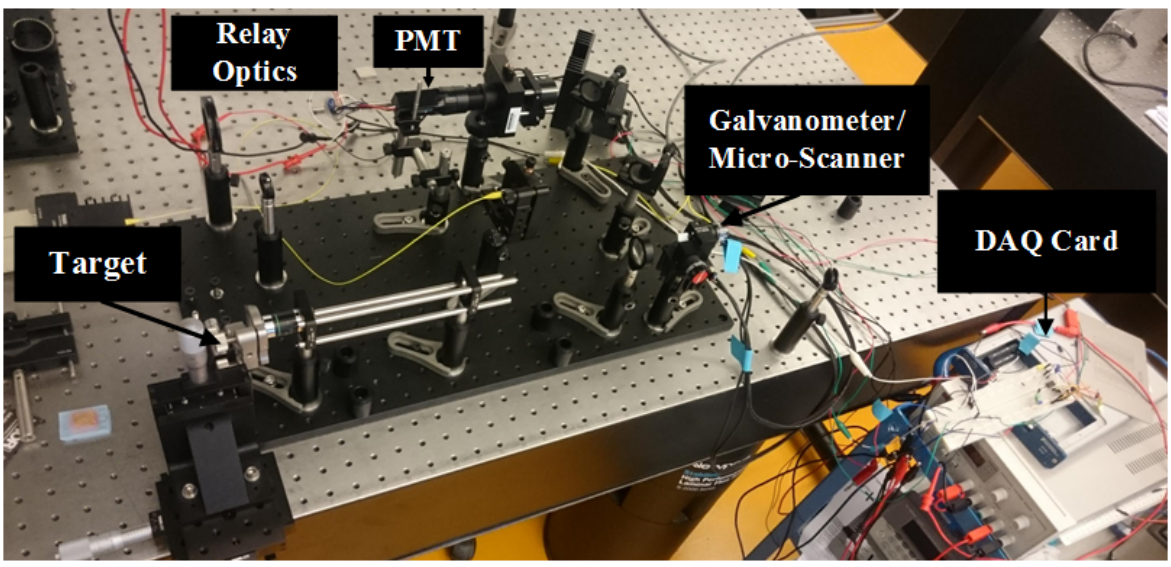

Figure 4.1. Test Setup.

After the system was assembled, it was tested on USAF-1951 resolution target which can be seen in Figure 4.2. The image which is acquired by utilized galvanometer is shown in Figure 4.3.

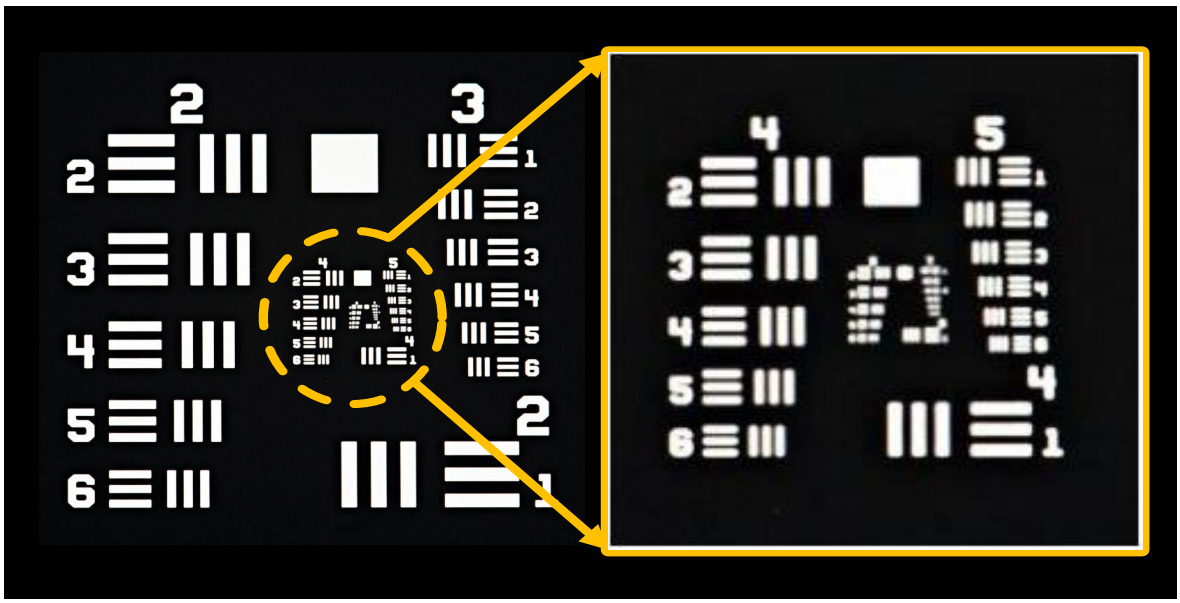

Figure 4.2. USAF-1951 Resolution Target and Scanned Part of the USAF Resolution Target.

The system is also tested on biological samples such as onion skin, chicken skin, yeast cells, bacteria cells and red blood cells. Acquired images are presented in the following part.

By using optical sectioning ability of LSCM, images acquired from 16 different layers of an onion epidermal cell is shown in Figure 4.4. Depth of each layer is approximately 20-30 μm and FOV is $500 \times 500 \mu m$ for each image. Onion cells and cell walls can be seen in acquired images. Moving from outside to inside these structures become more visible.

System is also tested on yeast cells which are obtained from laboratory of Istanbul Bilgi University Genetic Engineering department. Yeast cells are viewed under LSCM and light microscope. Results can be seen in Figure 4.5(a) and Figure 4.5(b) respectively. Diameters of the yeast cells are between 2-10 μm can be seen as white spots in Figure 4.5(b).

Designed LSCM system is also tested on chicken skin sample. Firstly, images acquired from Vivascope 3000 commercial reflectance microscope which is already in use at Samatya Training and Research Hospital to make comparison between acquired

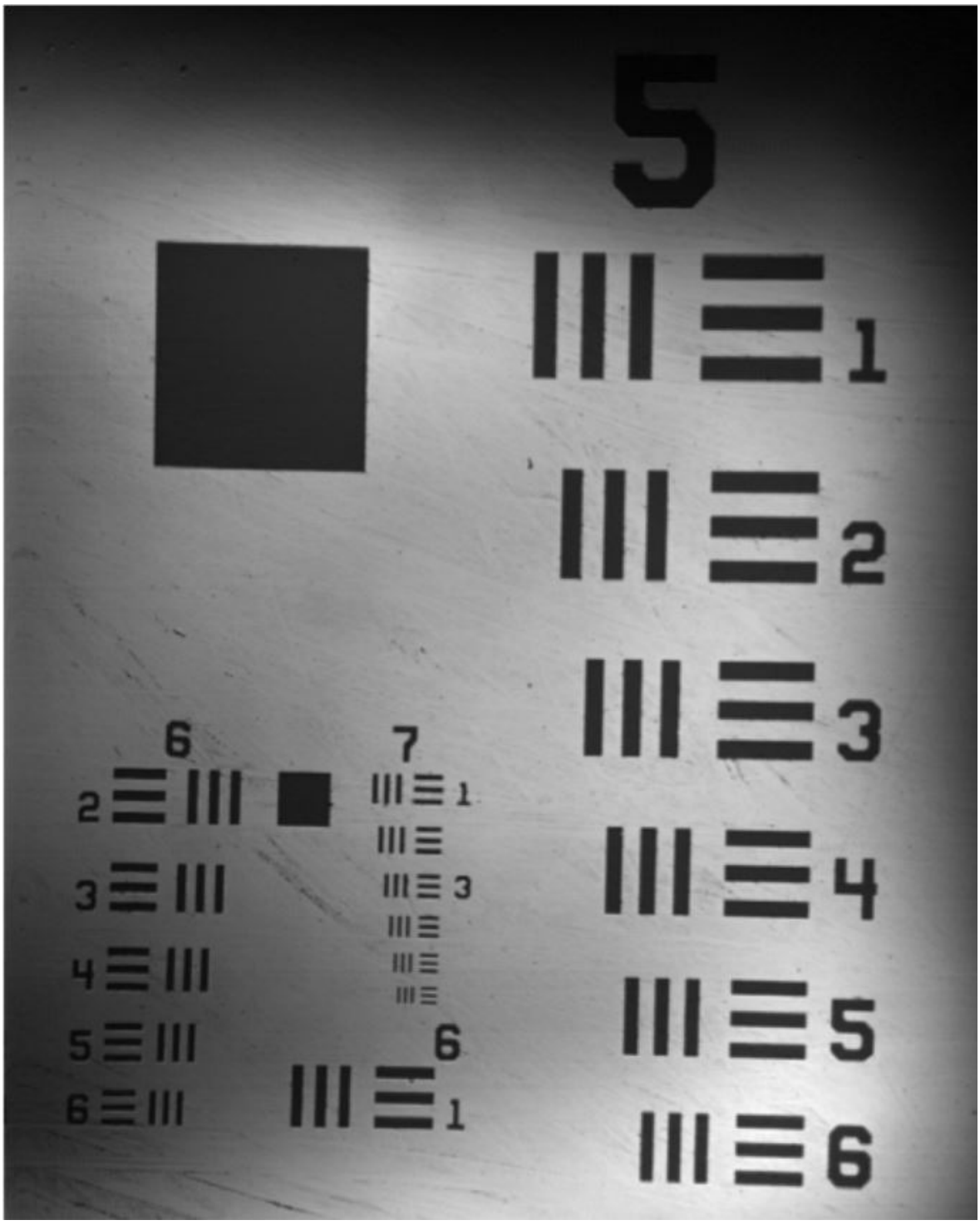

Figure 4.3. Acquired Image From the Resolution Target.

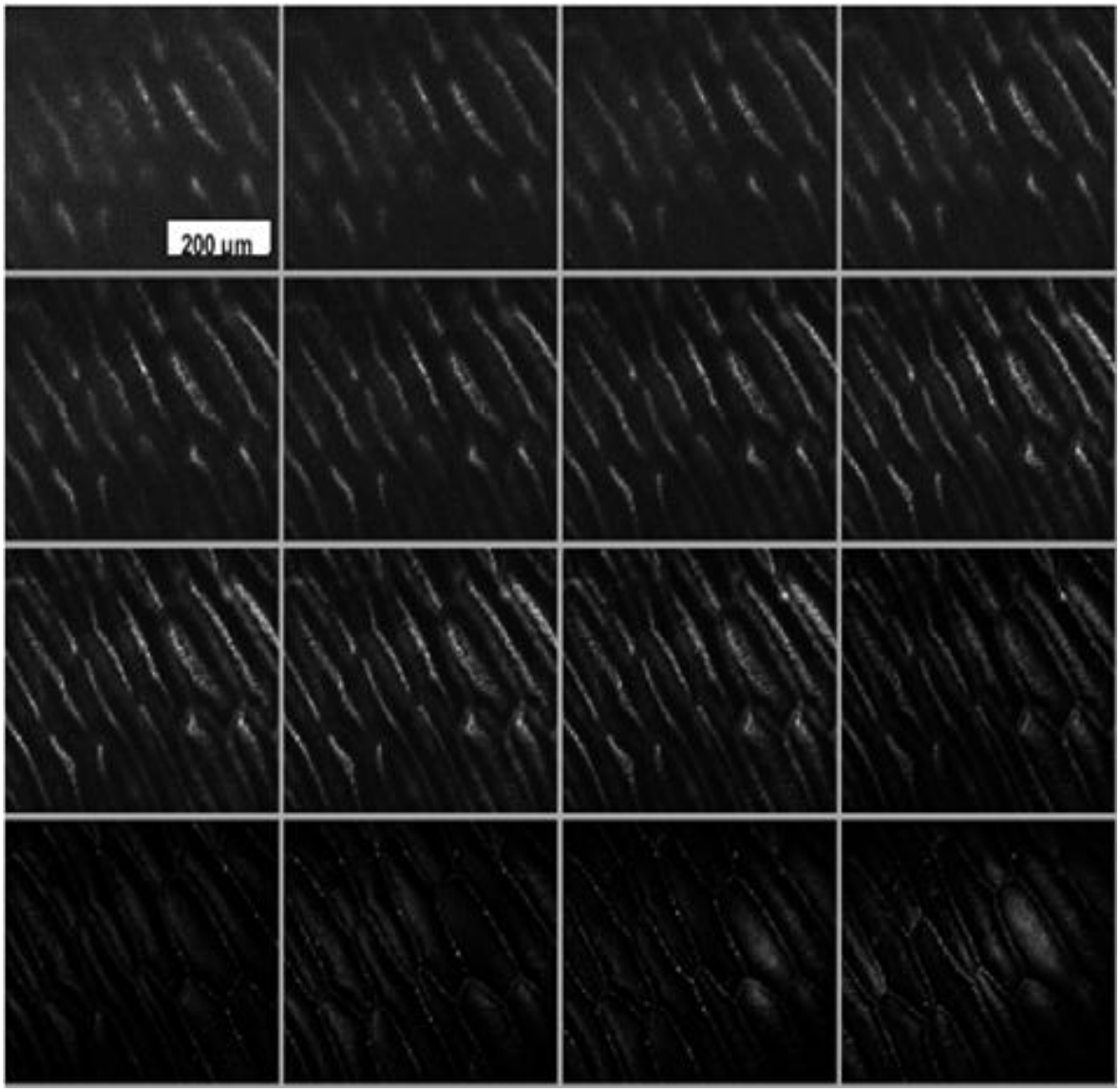

Figure 4.4. Acquired Images from 16 Different Layers of Onion Skin.

images from Vivascope 3000 and designed LSCM system. Starting from outside of the sample, images are acquired till 100 μm depth. Acquired image can be seen in Figure 4.6(b). Afterwards, image of the same sample is acquired by designed LSCM system. Nothing applied (i.e. dye) on the sample before imaging. In image which are acquired by Vivascope 3000, chicken skin cells' diameters are varying between 20-25 μm and their shape is like hexagon. In some regions of image which is obtained by LSCM system, these hexagonal cells can be partially seen.

If galvanometer is driven by slower frequencies resolution of acquired image can be increased. In order to show that, acquired images from two different layers of a

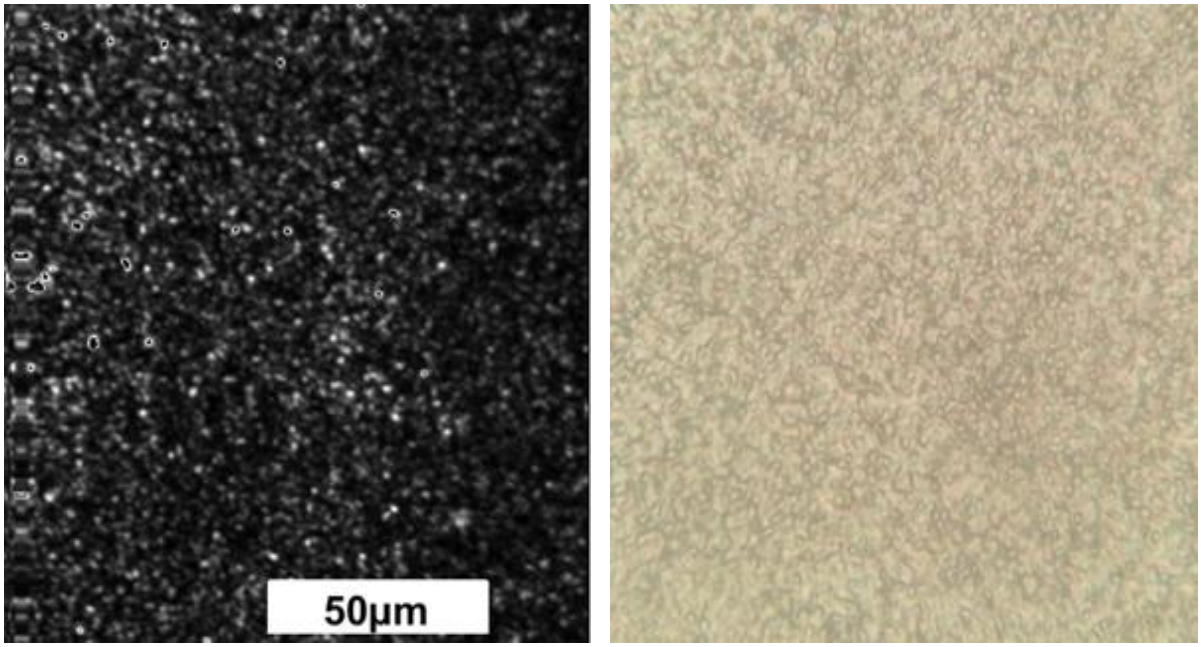

(a) (b)

Figure 4.5. Yeast Cells a) Under LSCM b) Under Light Microscope.

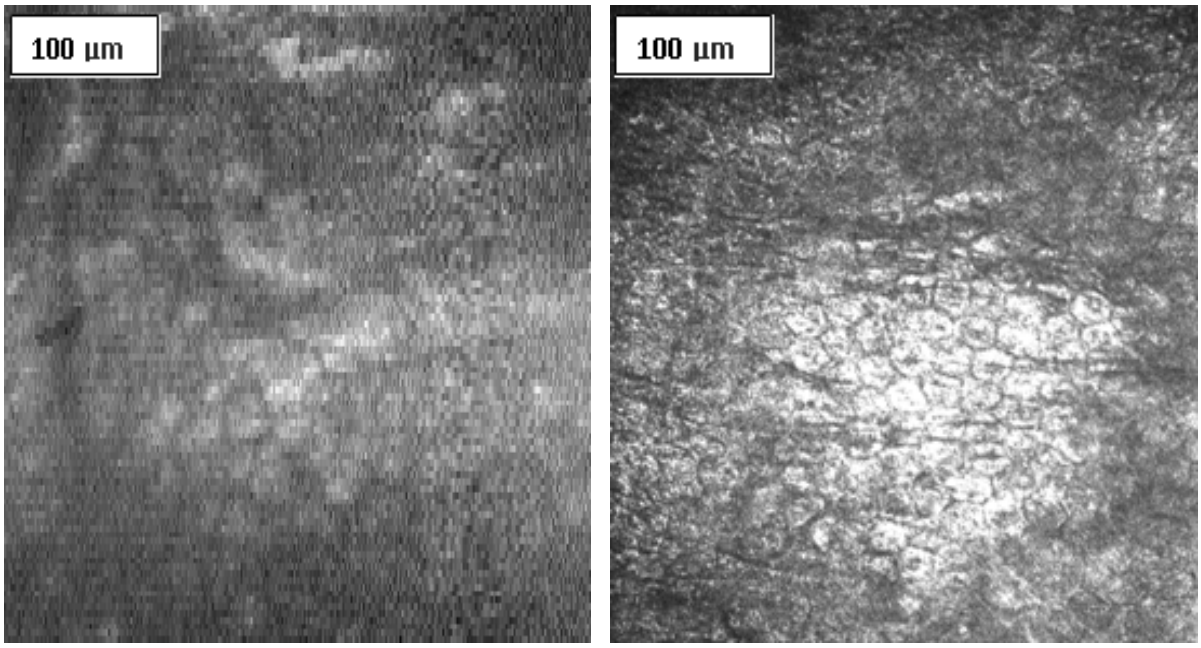

(a) (b)

Figure 4.6. Chicken Skin Sample Under a) LSCM b) Vivascope 3000.

onion skin is shown in Figure 4.7. When Figure 4.7 is compared with Figure 4.4, quality difference between them can be seen. However, driving galvanometer with slower frequencies decreases FPS value. Therefore, it conflicts with real time image acquisition objective of the system.

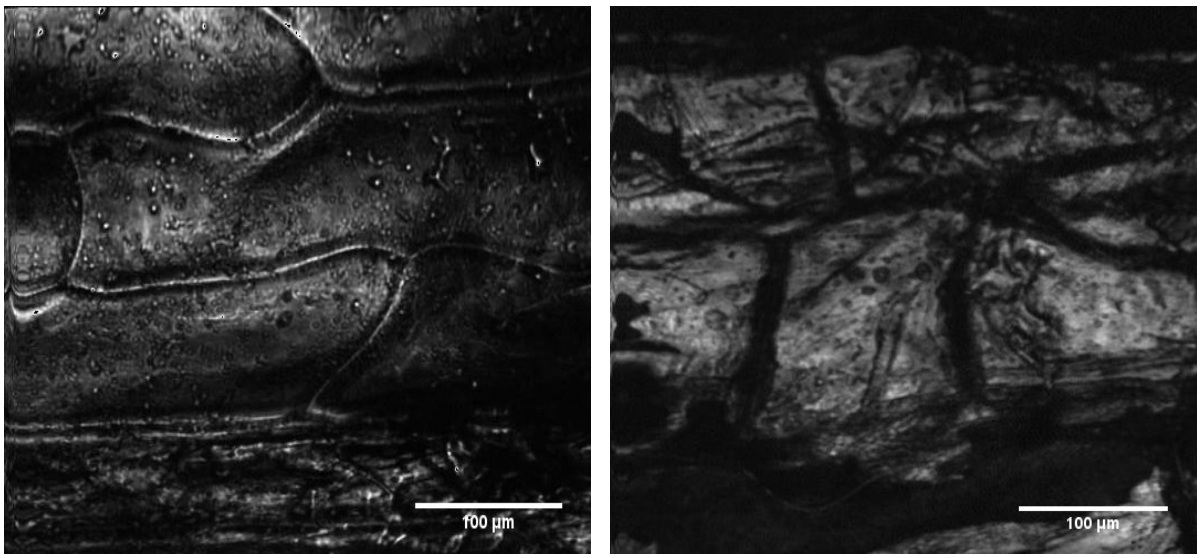

(a) (b)

Figure 4.7. Images Taken From Two Different Layers of an Onion Epidermal Cell.

In Figure 4.8, an image which shows bacteria cells under LSCM system can be seen. Each bacteria cell nearly have a diameter of 2 µm. Nevertheless, they can be seen with designed LSCM system clearly. Additionally, an image of red blood cells can be seen in Figure 4.9.

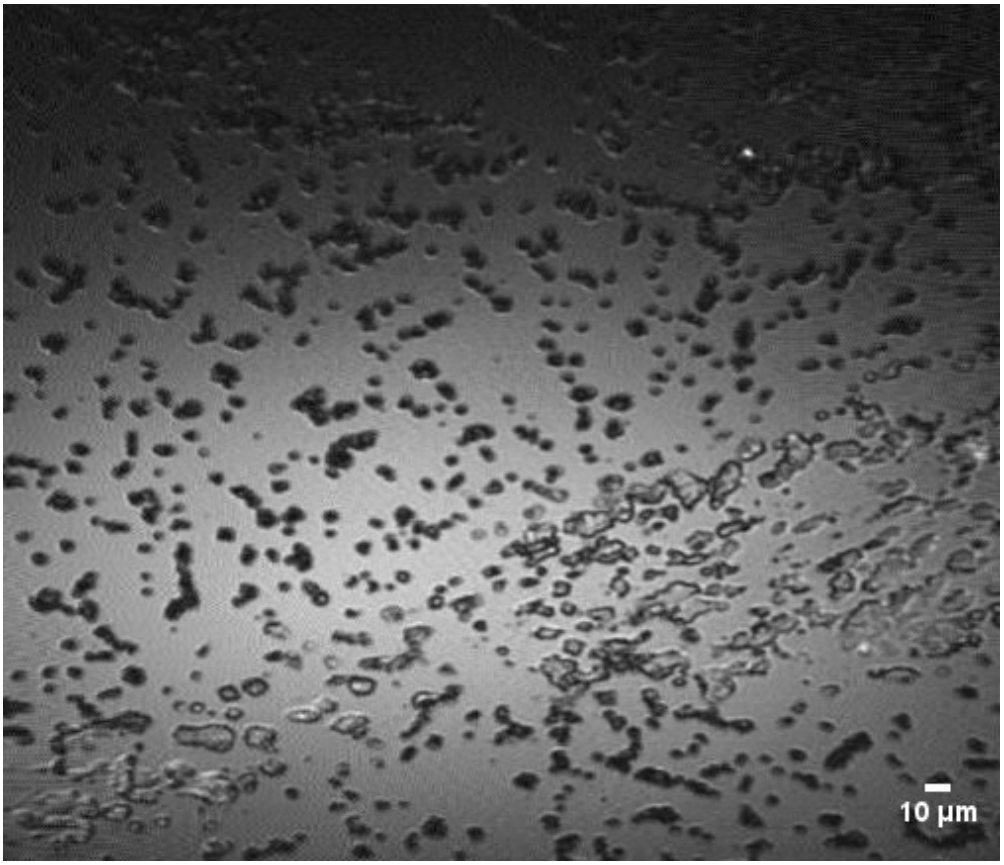

Figure 4.8. Bacteria Cells Under LSCM System.

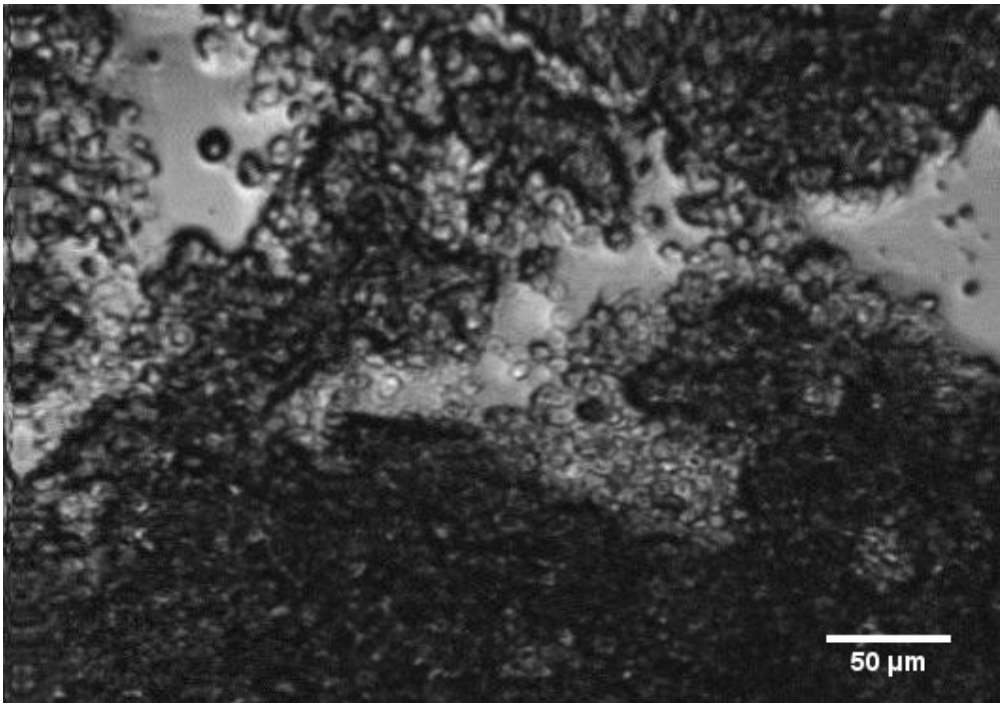

Figure 4.9. Red Blood Cells Under LSCM System.

Previous results are images taken from LSCM system by using raster scanning method. Lissajous scanning method is also employed in image acquisition process. It is tested on USAF 1951 resolution target. Resulting images can be seen in Figure 4.10 and Figure 4.11. Resulting image of Lissajous scanning with 3D micro-scanner is given in Figure 4.12. Because of low FOV, only a small part of the resolution target can be seen in Figure 4.12

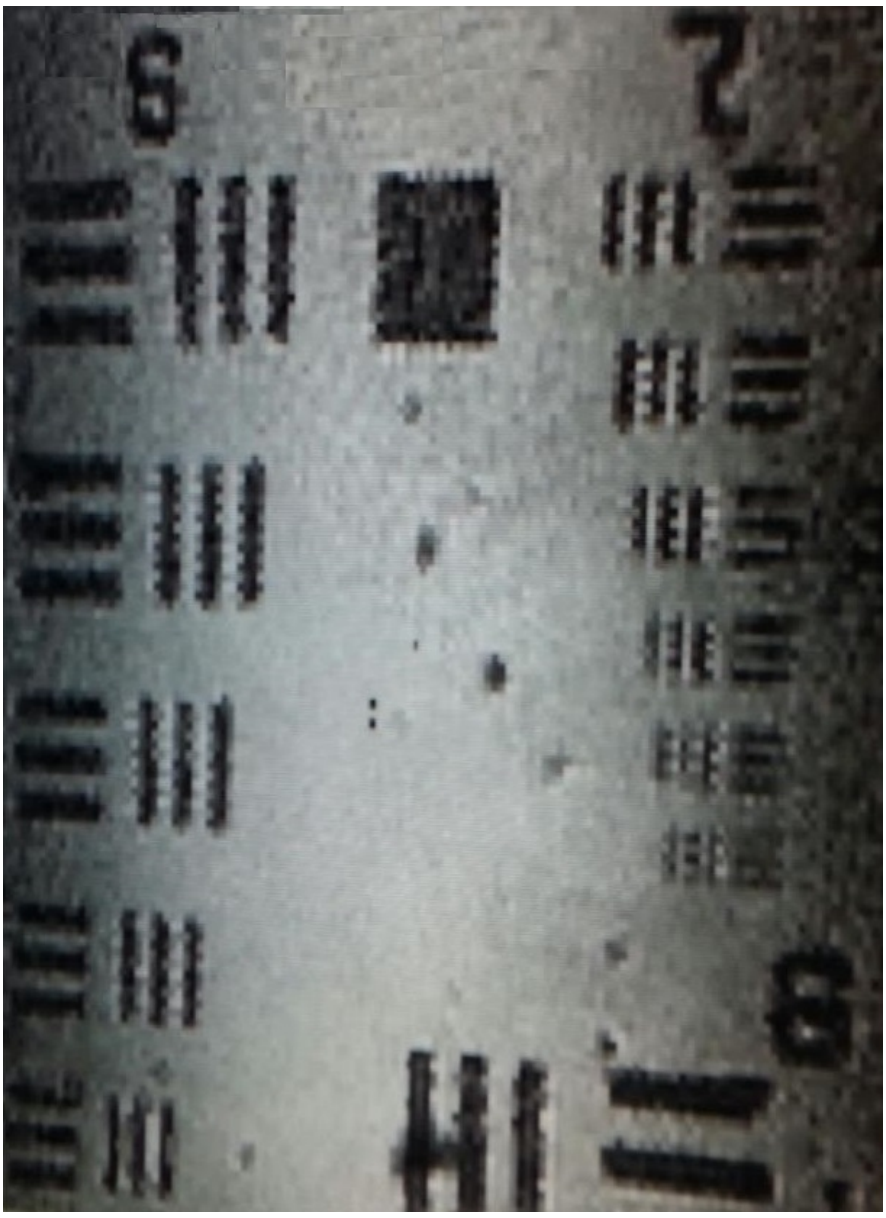

Figure 4.10. Acquired Image from Resolution Target by Using Lissajous Scanning with Frequency Values $f_x = 101$ Hz and $f_y = 100$ Hz.

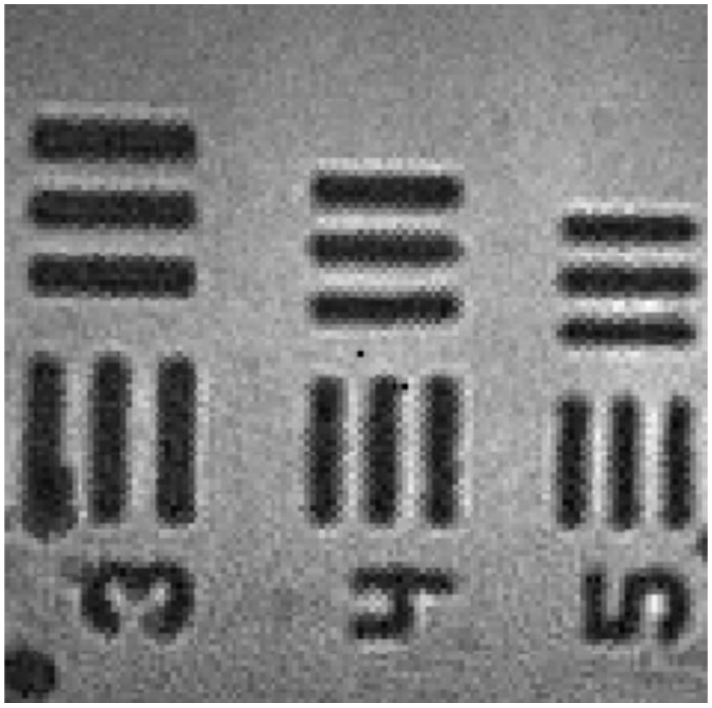

Figure 4.11. Resulting Image of Lissajous Scanning on Resolution Target with Frequency Values $f_x = 101$ Hz and $f_y = 100$ Hz.

Figure 4.12. Resulting Image of Lissajous Scanning with 3D Printed Micro-Scanner on Resolution Target with Frequency Values $f_x = 238$ Hz and $f_y = 113$ Hz.

4.2. Results of Denoising Process

Denoising experiments firstly conducted on white Gaussian noise with standard deviation $\sigma = 25$ added 512×512 "Lena" image which can be seen in Figure 4.13, to measure success of denoising methods. Aforementioned methods are applied on noisy image afterwards. The reason for that is to calculate peak signal-to-noise ratio (PSNR) properly for each method. There is no reference image to calculate PSNR for acquired images with LSCM system. They can be already noisy images and judging methods based on calculations which are done based on that images may cloud our judgement about which thresholding method or wavelet type is the most successful one.

(a) (b)

Figure 4.13. a) Original Lena Image (512x512) b) Noisy Lena Image $\sim N(0, \sigma^2)$ $\sigma = 25$.

Five different wavelets which are used widely are employed for wavelet decomposition. These wavelets are daubechies (db4, db8) and symlet (sym4, sym8, sym15) wavelets. In experiments, it has been seen that three level wavelet decomposition gives best PSNR values. Using greater level of decomposition decreases effectiveness and increase processing time. Decomposition level is selected as two in experiments. PSNR

which is used to measure success of different methods can be expressed as:

$$PSNR = 10 \log_1 0 \frac{255^2}{MSE} \tag{4.1}$$

where 255 is maximum pixel value of image and MSE is the mean square error between the original and denoised image. Formula for MSE is given in Eq. 3.21. For evaluation, PSNR difference ($PSNR_{\text{diff}}$) between noisy image and denoised image is used. The greatest PSNR value in each table indicates which method is the best. Best results are indicated with yellow color. Resulting images of best methods can be seen in figures which are placed below of corresponding tables which shows results for global median estimator (GME), level dependent median estimator (LDME) and detail dependent median estimator (DDME) respectively.

Table 4.1. $PSNR_{\text{diff}}$ Values for GME (dB).

		Wavelet Types				
		Db4	Db8	Sym4	Sym8	Sym15
Soft Thresholding	Universal	5, 4916	5.5478	5.4819	5.5407	5.5749
	SURE	5.4941	5.5489	5.4849	5.5412	5.5773
Hard Thresholding	Universal	5.4916	5.5475	5.4819	5.5407	5.5748
	SURE	5.4024	5.2347	5.2519	5.1606	5.4022

Resulting image which is obtained by applying noisy image the denoising method with GME and Sym15 wavelet is shown in Figure 4.14.

Figure 4.14. Resulting Denoised Image of GME and Sym15 Wavelet Method $PSNR_{\text{diff}} = 5.5773\ dB$.

Table 4.2. $PSNR_{\text{diff}}$ Values for LDME (dB).

		Wavelet Types				
		Db4	Db8	Sym4	Sym8	Sym15
Soft Thresholding	Universal	3.2039	3.1901	3.2116	3.2664	3.3021
	SURE	2.5327	2.5486	2.5772	2.5980	2.5726
Hard Thresholding	Universal	3.0765	3.0726	3.1293	3.1700	3.1179
	SURE	1.3647	1.4024	1.4114	1.4244	1.3920

Resulting image which is obtained by applying noisy image the denoising method with LDME and Sym15 wavelet is shown in Figure 4.15.

Figure 4.15. Resulting Denoised Image of LDME and Sym15 Wavelet Method $PSNR_{\text{diff}} = 3.3021\ dB$.

Table 4.3. $PSNR_{\text{diff}}$ Values for DDME (dB).

		Wavelet Types				
		Db4	Db8	Sym4	Sym8	Sym15
Soft Thresholding	Universal	5.8883	5.9091	5.9633	6.0797	6.1551
	SURE	8.7440	8.7501	8.8222	9.0126	8.9981
Hard Thresholding	Universal	6.7052	6.5857	6.7507	6.9207	6.9249
	SURE	7.0549	7.0102	7.0554	6.9316	7.0080

Resulting image which is obtained by applying noisy image the denoising method with DDME and Sym8 wavelet is shown in Figure 4.16.

Figure 4.16. Resulting Denoised Image of DDME and Sym8 Wavelet Method $PSNR_{\text{diff}} = 9.0126\ dB$.

Considering the results above, the most successful method is the method with Sym8 wavelet, SURE, DDME, soft thresholding combination. However as presented in Figure 4.17, soft thresholding causes blur on image. Therefore, Sym8 wavelet, SURE, DDME and hard thresholding combination is applied onto images acquired with LSCM system from bacteria cells, red blood cells and onion epidermal samples. Results can be seen in Figure 4.18, Figure 4.19 and Figure 4.20 respectively. Noise standard deviation is estimated as one in the following results.

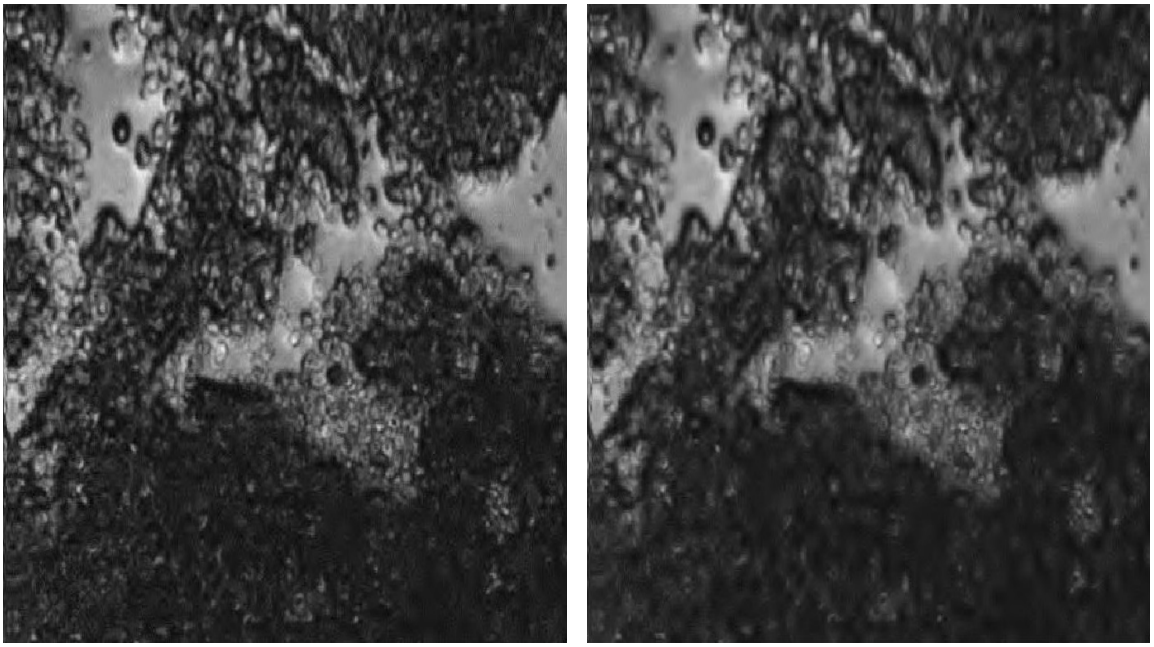

(a) (b)

Figure 4.17. Denoising Results with a) Hard Thresholding b) Soft Thresholding

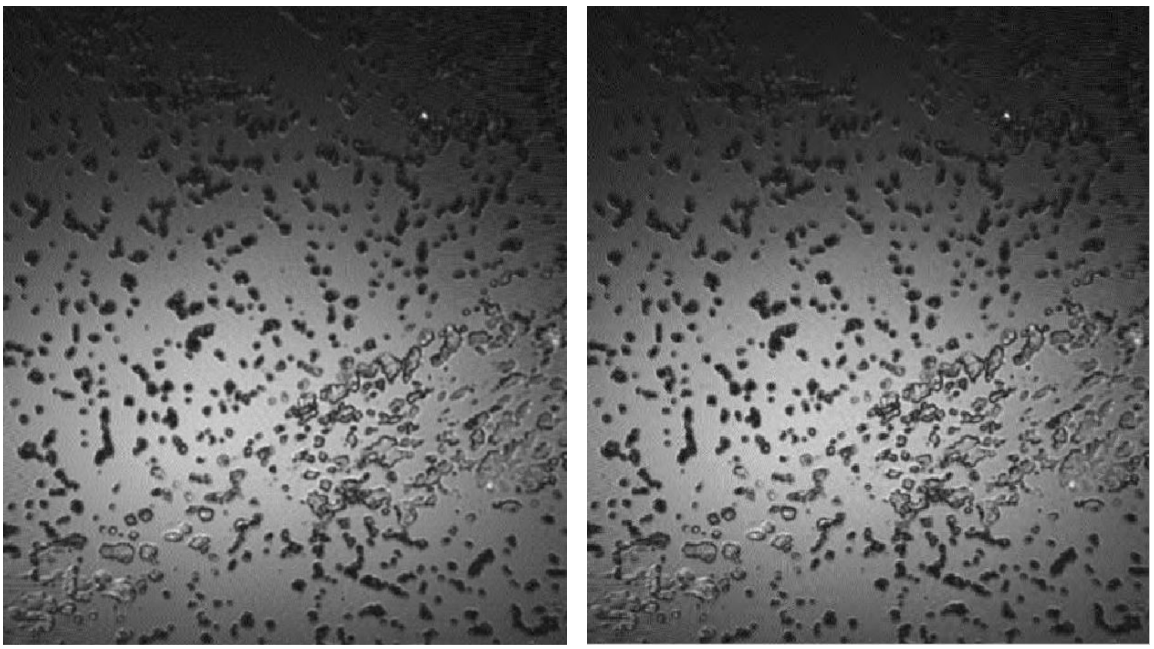

(a) (b)

Figure 4.18. a) Original Image Acquired From Bacteria Cells Sample b) Denoised Image

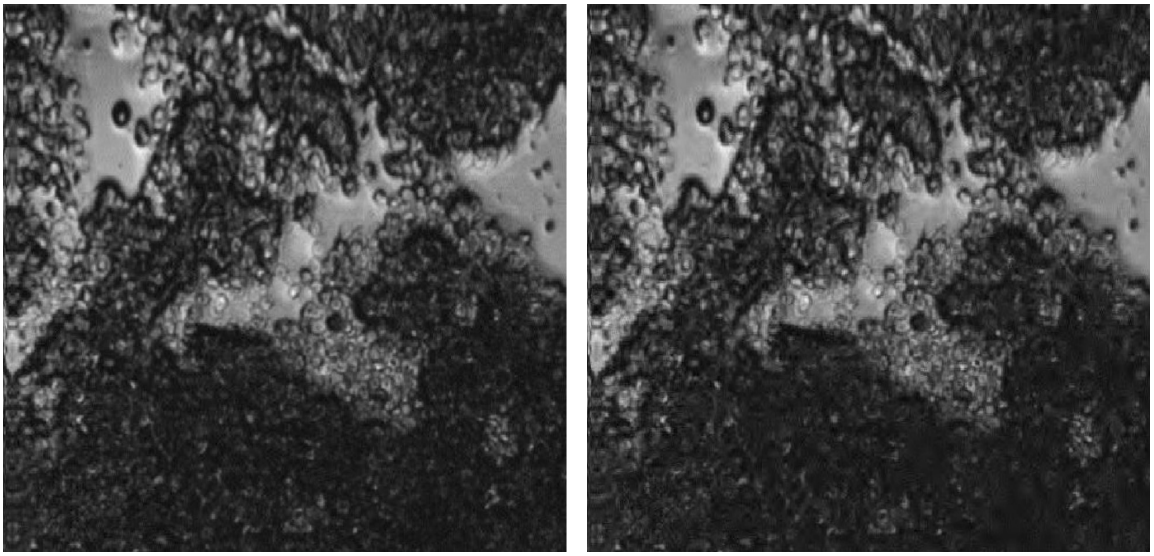

(a) (b)

Figure 4.19. a) Original Image Acquired From Red Blood Cells Sample b) Denoised Image

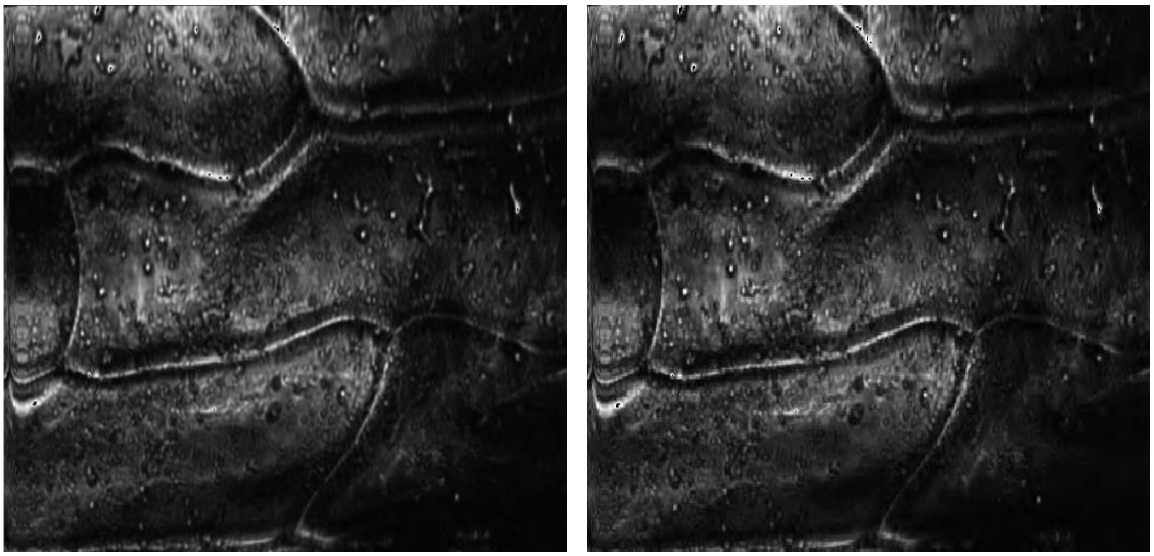

(a) (b)

Figure 4.20. a) Original Image Acquired From Onion Epidermal Sample b) Denoised Image

5. CONCLUSION

In this thesis, a novel laser scanning confocal microscopy system is presented. The LSCM system is designed in two different configurations namely (1) micro-scanner based LSCM and (2) galvanometer based LSCM. Purpose of the overall system is to scan a target object with scanning units (i.e. micro-scanner, galvanometer) by using raster and Lissajous scanning methods and display the resulting image on a GUI. A DAQ Card is employed for controlling the microscope system. A special software is written in MATLAB program for the DAQ Card. The software realizes two main operations; actuation signal generation and image acquisition. In the actuation signal part, a signal is generated from the GUI to control actuation of the scanning units. On the GUI, various parameters can be set and different types of signals can be combined to generate different types of actuation signals. In micro-scanner based LSCM system, an actuation signal which is composed of two sinusoidal signals (i.e. slow and fast frequencies of the micro-scanner), is generated from an output channel of DAQ card to create a magnetic field which results in scanning motion of the micro-scanner. The current supplied by the DAQ card is amplified for creating sufficient magnetic field for actuation of the micro-scanner. Additionally, amplification of the actuation signal is a necessity for increasing and achieving a satisfactory filed-of-view. Therefore, a power amplifier circuit with LM 386 integrated circuit is designed and added to the output of the DAQ card analog output channel. The electro-coil placed near to the micro-scanner is driven with the amplified actuation signal. On the other hand, in galvanometer based LSCM system, two separate output channels of DAQ card is utilized to drive galvanometer. In order to scan target with raster scanning method, two sawtooth waves are employed. For Lissajous scanning method, two sinusoidal waves are generated from DAQ card.

In the image acquisition part, a PMT collects laser beams which are reflected from the scanning target; and it generates electrical current values according to power of the reflected laser beams. The electrical current values are converted to voltage values on a resistor. Converted voltage values are acquired by the DAQ Card in a serial

manner. The acquired voltage values are mapped between 0 and 255 according to previously calibrated maximum and minimum voltage values. According to the dimension information of the scan, an image is constructed by gathering all of the pixels belong to the image. Algorithms of raster and Lissajous scanning methods are presented. Successful operation of the proposed system is demonstrated by constructing images from USAF 1951 resolution target.In addition to that, images acquired from specimens like yeast cells, onion skin, chicken skin, red blood cells, bacteria cells are provided. In the conducted experiments, it has been seen that maximum resolution of images which are acquired by utilizing galvanometer can be under 1 μm both in horizontal and vertical axis. Additionally, maximum FOV is calculated as $1000 \times 1000\ \mu m^2$. FPS value for the system is calculated as 0.5. In order to improve quality of resulting images of LSCM system, denoising is applied to the images by using wavelet transform method. Thresholding methods which are universal and SURE thresholding are compared along with median estimation methods which are GME, LDME and DDME by using Db4, Db8, Sym4, Sym8 and Sym15 wavelets. In the conducted experiments, the method with Sym8 wavelet, SURE and DDME combination gave the best results in terms of PSNR. Therefore, the method is applied to resulting images of LSCM system. However, hard thresholding method is used instead of soft thresholding method. Denoised images are presented.

Comparison between images taken with proposed LSCM system and commercial microscope systems are presented. The experimental results show that the proposed system can be utilized for medical diagnosis.

REFERENCES

1. Mu, X., W. Sun, H. Feng, A. Yu, K. W. S. Chen, C. Y. Fu and M. Olivo, "MEMS micromirror integrated endoscopic probe for optical coherence tomography bioimaging", *Sensors and Actuators A: Physical*, Vol. 168, No. 1, pp. 202–212, 2011.

2. Sun, J., S. Guo, L. Wu, L. Liu, S.-W. Choe, B. S. Sorg and H. Xie, "3D in vivo optical coherence tomography based on a low-voltage, large-scan-range 2D MEMS mirror", *Optics express*, Vol. 18, No. 12, pp. 12065–12075, 2010.

3. Kim, K. H., J. A. Burns, J. J. Bernstein, G. N. Maguluri, B. H. Park and J. F. de Boer, "In vivo 3D human vocal fold imaging with polarization sensitive optical coherence tomography and a MEMS scanning catheter", *Optics express*, Vol. 18, No. 14, pp. 14644–14653, 2010.

4. Flusberg, B. A., J. C. Jung, E. D. Cocker, E. P. Anderson and M. J. Schnitzer, "In vivo brain imaging using a portable 3.9? gram two-photon fluorescence microendoscope", *Optics letters*, Vol. 30, No. 17, pp. 2272–2274, 2005.

5. Helmchen, F., W. Denk and J. N. Kerr, "Miniaturization of two-photon microscopy for imaging in freely moving animals", *Cold Spring Harbor Protocols*, Vol. 2013, No. 10, pp. pdb–top078147, 2013.

6. Zhang, C. C., W. B. Foster, R. D. Downey, C. L. Arrasmith and D. L. Dickensheets, "Dynamic performance of MEMS deformable mirrors for use in an active/adaptive two-photon microscope", *SPIE BiOS*, pp. 97170G–97170G, International Society for Optics and Photonics, 2016.

7. Ra, H., W. Piyawattanametha, Y. Taguchi, D. Lee, M. J. Mandella and O. Solgaard, "Two-dimensional MEMS scanner for dual-axes confocal microscopy", *Journal of Microelectromechanical systems*, Vol. 16, No. 4, p. 969, 2007.

8. Wang, T. D., C. H. Contag, M. J. Mandella, N. Chan and G. S. Kino, "Dual-axes confocal microscopy with post-objective scanning and low-coherence heterodyne detection", *Optics letters*, Vol. 28, No. 20, pp. 1915–1917, 2003.

9. Ra, H., W. Piyawattanametha, E. Gonzalez-Gonzalez, M. J. Mandella, G. S. Kino, O. Solgaard, D. Leake, R. L. Kaspar, A. Oro and C. H. Contag, "In vivo imaging of human and mouse skin with a handheld dual-axis confocal fluorescence microscope", *Journal of Investigative Dermatology*, Vol. 131, No. 5, pp. 1061–1066, 2011.

10. Minsky, M., "Microscopy apparatus", `http://www.google.com/patents/US3013467`, Dec. 19 1961, uS Patent 3,013,467, accessed at May 2016.

11. Pawley, J. and B. R. Masters, "Handbook of biological confocal microscopy", *Optical Engineering*, Vol. 35, No. 9, pp. 2765–2766, 1996.

12. Lundstedt, C., H. Stridbeck, R. Andersson, K.-G. Tranberg and Å. Andrén-Sandberg, "Tumor seeding occurring after fine-needle biopsy of abdominal malignancies", *Acta Radiologica*, Vol. 32, No. 6, pp. 518–520, 1991.

13. Kumar, K., R. Avritscher, Y. Wang, N. Lane, D. C. Madoff, T.-K. Yu, J. W. Uhr and X. Zhang, "Handheld histology-equivalent sectioning laser-scanning confocal optical microscope for interventional imaging", *Biomedical microdevices*, Vol. 12, No. 2, pp. 223–233, 2010.

14. Wilson, T., "Confocal microscopy", *Academic Press: London, etc*, Vol. 426, pp. 1–64, 1990.

15. Dickensheets, D. and G. Kino, "Micromachined scanning confocal optical microscope", *Optics letters*, Vol. 21, No. 10, pp. 764–766, 1996.

16. Shin, H.-J., M. C. Pierce, D. Lee, H. Ra, O. Solgaard and R. Richards-Kortum, "Fiber-optic confocal microscope using a MEMS scanner and miniature objective lens", *Optics express*, Vol. 15, No. 15, pp. 9113–9122, 2007.

17. Polglase, A. L., W. J. McLaren, S. A. Skinner, R. Kiesslich, M. F. Neurath and P. M. Delaney, "A fluorescence confocal endomicroscope for in vivo microscopy of the upper-and the lower-GI tract", *Gastrointestinal endoscopy*, Vol. 62, No. 5, pp. 686–695, 2005.

18. Knittel, J., L. Schnieder, G. Buess, B. Messerschmidt and T. Possner, "Endoscope-compatible confocal microscope using a gradient index-lens system", *Optics Communications*, Vol. 188, No. 5, pp. 267–273, 2001.

19. Paddock, S. W., "Principles and practices of laser scanning confocal microscopy", *Molecular biotechnology*, Vol. 16, No. 2, pp. 127–149, 2000.

20. Minsky, M., "Memoir on inventing the confocal scanning microscope", *Scanning*, Vol. 10, No. 4, pp. 128–138, 1988.

21. Swedlow, J. R., K. Hu, P. D. Andrews, D. S. Roos and J. M. Murray, "Measuring tubulin content in Toxoplasma gondii: a comparison of laser-scanning confocal and wide-field fluorescence microscopy", *Proceedings of the National Academy of Sciences*, Vol. 99, No. 4, pp. 2014–2019, 2002.

22. Xie, Z., S. Jiao, H. F. Zhang and C. A. Puliafito, "Laser-scanning optical-resolution photoacoustic microscopy", *Optics letters*, Vol. 34, No. 12, pp. 1771–1773, 2009.

23. Mu, X., G. Zhou, H. Yu, Y. Du, H. Feng, J. M. L. Tsai and F. S. Chau, "Compact MEMS-driven pyramidal polygon reflector for circumferential scanned endoscopic imaging probe", *Optics express*, Vol. 20, No. 6, pp. 6325–6339, 2012.

24. Aljasem, K., L. Froehly, A. Seifert and H. Zappe, "Scanning and tunable micro-optics for endoscopic optical coherence tomography", *Microelectromechanical Systems, Journal of*, Vol. 20, No. 6, pp. 1462–1472, 2011.

25. Pan, Y., H. Xie and G. K. Fedder, "Endoscopic optical coherence tomography based on a microelectromechanical mirror", *Optics letters*, Vol. 26, No. 24, pp.

1966–1968, 2001.

26. Jung, W., J. Zhang, L. Wang, P. Wilder-Smith, Z. Chen, D. T. McCormick and N. C. Tien, "Three-dimensional optical coherence tomography employing a 2-axis microelectromechanical scanning mirror", *Selected Topics in Quantum Electronics, IEEE Journal of*, Vol. 11, No. 4, pp. 806–810, 2005.

27. Zara, J. M. and P. E. Patterson, "Polyimide amplified piezoelectric scanning mirror for spectral domain optical coherence tomography", *Applied physics letters*, Vol. 89, No. 26, p. 263901, 2006.

28. Mitsui, T., Y. Takahashi and Y. Watanabe, "A 2-axis optical scanner driven non-resonantly by electromagnetic force for OCT imaging", *Journal of Micromechanics and Microengineering*, Vol. 16, No. 11, p. 2482, 2006.

29. Hah, D., S. Huang, H. Nguyen, H. Chang, J.-C. Tsai, M. C. Wu and H. Toshiyoshi, "Low voltage MEMS analog micromirror arrays with hidden vertical comb-drive actuators", *2002 Solid-State Sensor, Actuator and Microsystems Workshop (Hilton Head 2002)*, pp. 2–6, 2002.

30. Park, S. and E. Abdel-Rahman, "Low voltage electrostatic actuation and displacement measurement through resonant drive circuit", *ASME 2012 International Design Engineering Technical Conferences and Computers and Information in Engineering Conference*, pp. 119–126, American Society of Mechanical Engineers, 2012.

31. Xu, Z., S. Kolev and E. Todorov, "Design, optimization, calibration, and a case study of a 3d-printed, low-cost fingertip sensor for robotic manipulation", *Robotics and Automation (ICRA), 2014 IEEE International Conference on*, pp. 2749–2756, IEEE, 2014.

32. Kesner, S. B. and R. D. Howe, "Design principles for rapid prototyping forces sensors using 3-D printing", *Mechatronics, IEEE/ASME Transactions On*, Vol. 16, No. 5, pp. 866–870, 2011.

33. Willis, K., E. Brockmeyer, S. Hudson and I. Poupyrev, "Printed optics: 3D printing of embedded optical elements for interactive devices", *Proceedings of the 25th annual ACM symposium on User interface software and technology*, pp. 589–598, ACM, 2012.

34. Wu, S.-Y., C. Yang, W. Hsu and L. Lin, "3D-printed microelectronics for integrated circuitry and passive wireless sensors", *Microsystems & Nanoengineering*, Vol. 1, 2015.

35. Shemelya, C., F. Cedillos, E. Aguilera, E. Maestas, J. Ramos, D. Espalin, D. Muse, R. Wicker and E. MacDonald, "3D printed capacitive sensors", *SENSORS, 2013 IEEE*, pp. 1–4, IEEE, 2013.

36. Kong, Y. L., I. A. Tamargo, H. Kim, B. N. Johnson, M. K. Gupta, T.-W. Koh, H.-A. Chin, D. A. Steingart, B. P. Rand and M. C. McAlpine, "3D printed quantum dot light-emitting diodes", *Nano letters*, Vol. 14, No. 12, pp. 7017–7023, 2014.

37. Oyman, H. A., Y. D. Gokdel, O. Ferhanoglu and A. D. Yalcinkaya, "3D Printed MEMS Scanners", *Sensors and Actuators*, Vol. submitted, 2016.

38. Lissajous, J., "Note sur un nouveau moyen de mettre en évidence le mouvement vibratoire des corps", *CR Hebd. Seances Acad. Sci*, Vol. 41, pp. 93–95, 1855.

39. Hoy, C. L., N. J. Durr and A. Ben-Yakar, "Fast-updating and nonrepeating Lissajous image reconstruction method for capturing increased dynamic information", *Applied optics*, Vol. 50, No. 16, pp. 2376–2382, 2011.

40. Hoy, C. L., N. J. Durr, P. Chen, W. Piyawattanametha, H. Ra, O. Solgaard and A. Ben-Yakar, "Miniaturized probe for femtosecond laser microsurgery and two-photon imaging", *Optics express*, Vol. 16, No. 13, pp. 9996–10005, 2008.

41. Liu, T.-M., M.-C. Chan, I.-H. Chen, S.-H. Chia and C.-K. Sun, "Miniaturized multiphoton microscope with a 24Hz frame-rate", *Optics express*, Vol. 16, No. 14,

pp. 10501–10506, 2008.

42. Bazaei, A., Y. K. Yong and S. R. Moheimani, "High-speed Lissajous-scan atomic force microscopy: Scan pattern planning and control design issues", *Review of Scientific Instruments*, Vol. 83, No. 6, p. 063701, 2012.

43. Tuma, T., J. Lygeros, V. Kartik, A. Sebastian and A. Pantazi, "High-speed multiresolution scanning probe microscopy based on Lissajous scan trajectories", *Nanotechnology*, Vol. 23, No. 18, p. 185501, 2012.

44. Daubechies, I. *et al.*, *Ten lectures on wavelets*, Vol. 61, SIAM, 1992.

45. Wikipedia, "Photomultiplier — Wikipedia, The Free Encyclopedia", `https://en.wikipedia.org/w/index.php?title=Photomultiplier&oldid=716363740`, accessed at May 2016.

46. Young, W. C. and R. G. Budynas, *Roark's formulas for stress and strain*, Vol. 7, McGraw-Hill New York, 2002.

47. Wikipedia, "Lissajous curve — Wikipedia, The Free Encyclopedia", `https://en.wikipedia.org/w/index.php?title=Lissajous_curve&oldid=723304226`, accessed at May 2016.

48. Zipfel, W. R., R. M. Williams and W. W. Webb, "Nonlinear magic: multiphoton microscopy in the biosciences", *Nature biotechnology*, Vol. 21, No. 11, pp. 1369–1377, 2003.

49. Donoho, D. L. and I. M. Johnstone, "Threshold selection for wavelet shrinkage of noisy data", *Engineering in Medicine and Biology Society, 1994. Engineering Advances: New Opportunities for Biomedical Engineers. Proceedings of the 16th Annual International Conference of the IEEE*, pp. A24–A25, IEEE, 1994.

50. Bultheel, A., "Wavelets with applications in signal and image processing", *Sep-*

tiembre de, pp. 157–162, 2003.

51. Chang, S. G., B. Yu and M. Vetterli, "Adaptive wavelet thresholding for image denoising and compression", *Image Processing, IEEE Transactions on*, Vol. 9, No. 9, pp. 1532–1546, 2000.

52. Lang, M., H. Guo, J. E. Odegard, C. S. Burrus and R. Wells Jr, "Noise reduction using an undecimated discrete wavelet transform", *Signal Processing Letters, IEEE*, Vol. 3, No. 1, pp. 10–12, 1996.

53. Abramovich, F. and Y. Benjamini, "Adaptive thresholding of wavelet coefficients", *Computational Statistics & Data Analysis*, Vol. 22, No. 4, pp. 351–361, 1996.

54. Nason, G. P., "Wavelet shrinkage using cross-validation", *Journal of the Royal Statistical Society. Series B (Methodological)*, pp. 463–479, 1996.

55. Donoho, D. L. and J. M. Johnstone, "Ideal spatial adaptation by wavelet shrinkage", *Biometrika*, Vol. 81, No. 3, pp. 425–455, 1994.

56. Ellinas, J., T. Mandadelis, A. Tzortzis and L. Aslanoglou, "Image de-noising using wavelets", *TEI of Piraeus Applied Research Review*, Vol. 9, No. 1, pp. 97–109, 2004.

57. Ismail, B. and A. Khan, "Image de-noising with a new threshold value using wavelets", *Journal of Data Science*, Vol. 10, pp. 259–270, 2012.

58. Vetterli, M. and J. Kovacevic, *Wavelets and subband coding*, LCAV-BOOK-1995-001, Prentice-hall, 1995.

59. Burrus, C. S., R. A. Gopinath and H. Guo, *Introduction to wavelets and wavelet transforms*, Prentice hall, 1997.

60. Strang, G. and T. Nguyen, *Wavelets and filter banks*, SIAM, 1996.

61. Mallat, S. G., "A theory for multiresolution signal decomposition: the wavelet representation", *Pattern Analysis and Machine Intelligence, IEEE Transactions on*, Vol. 11, No. 7, pp. 674–693, 1989.

62. Bala, E. and A. Ertüzün, "A multivariate thresholding technique for image denoising using multiwavelets", *EURASIP Journal on Applied Signal Processing*, Vol. 2005, pp. 1205–1211, 2005.

63. Stein, C. M., "Estimation of the mean of a multivariate normal distribution", *The annals of Statistics*, pp. 1135–1151, 1981.

64. Donoho, D. L. and I. M. Johnstone, "Adapting to unknown smoothness via wavelet shrinkage", *Journal of the american statistical association*, Vol. 90, No. 432, pp. 1200–1224, 1995.

65. Gumus, G., B. Sarioglu and Y. D. Gokdel, "An electronic control and image acquisition system for laser scanning microscopy", *2015 9th International Conference on Electrical and Electronics Engineering (ELECO)*, pp. 158–161, IEEE, 2015.